



**SETCOR**  
Conferences & Exhibitions

**The Joint International Conferences**

**Smart Materials and Surfaces**

**SMS 2018**

**European Graphene Forum**

**EGF 2018**

**NanoMedicine International Conference**

**NanoMed2018**

**Oct 23 to 25, 2018, Venice - Italy**

**Conference Proceedings**

DOI: <https://doi.org/10.26799/cp-sms-egf-nanomed2018>

# A Concept Study to Develop a Smart Sensory Textile Reinforced Concrete Pipe

Gözdem Dittel<sup>1</sup>, Kira Heins<sup>1</sup>, Thomas Gries<sup>1</sup>

<sup>1</sup>Institut fuer Textiltechnik of RWTH Aachen University

Otto-Blumenthal-Str. 1, 52074 Aachen, Germany, Gozdem.Dittel@ita.rwth-aachen.de

## Abstract

In this study, we aim to develop a concept for the construction of smart sensory textile reinforced concrete (TRC) pipes. The approach combines the advantages of thin walled alkali resistant (AR)-glass fiber based TRC with the structural-electrical properties of carbon rovings knitted into a textile grid. By integration of carbon rovings as sensory agents meaningful information regarding the functional and the structural health condition of the TRC load bearing element are provided.

This paper focuses on the production of a “smart TRC pipe” or rather on the fundamental considerations regarding wall thickness, positioning of the textile and effective placement of the functional fibers. Therefore a constructional concept is developed.

**Keywords:** Smart materials, textile reinforced concrete, water pipe, concept development

## 1. Introduction

There is a great demand in the world for low-cost and functional pipeline systems. This is due to the need to rehabilitate many pipes in use and on the other hand due to continuous development of new settlements which have to be connected to sewage and fresh water systems. As a result, the question arises of reducing the consumption of resources and the construction of cost-effective, safe, lightweight structures.

Nowadays used pipeline systems made of steel reinforced concrete are economical and sufficiently resistant, but large wall thicknesses and thus very heavy constructions are required to enable sufficient crack reduction and strength. In addition, the thick concrete cover is required to protect steel reinforcement from corrosion and as a result weakened structures. This bulkiness of the constructions considerably limits the application possibilities [1]. TRC counteracts these disadvantages. This building material enables the production of thin-walled and lightweight structures.

Furthermore, there has been a great interest in research and industry in the integration of sensor functions in components [2]. These smart materials promise costs and operational savings in manufacturing and transport, as well as in maintenance and repair [3].

The main interest in using TRC for this field of application is due to the resistance of the textile reinforcements regarding corrosion. As a result the required minimum concrete cover is lower compared to steel reinforced concrete. Hence, particularly light and thin-walled components with high surface quality can be produced. The use of concrete can be reduced by up to 80 % compared to conventional steel reinforced concrete structures. In addition, three-dimensional reinforcement structures in which the fibers are oriented in the direction of the present load [4].

This research aims to proof the usability of a smart textile material as reinforcement structure for concrete pipes. The integration of sensory fibers shall lead to a surveillance of mechanical load and damage as well as the penetration of liquid through the wall. In previous studies Goldfeld et al. [5] showed, that a drop of electrical resistance of integrated sensory fibers indicates a leakage.

The aspects that need to be taken into account when selecting building materials and designing them for use in pipelines are among others the expected internal and external loads, existing subsoil conditions, risk of corrosion from the surrounding soil, urban development structure of the supply area and the expenses for maintenance and operation [1]. For the design and dimensioning of a pipe, the occurring load is decisive. The actions are divided into loads during manufacture and transport (e.g. clamping, loading), during construction (e.g. backfilling, compaction, traffic loads) and during use (e.g. static, chemical and thermal loads). In residential water supply systems, constant environmental conditions are generally assumed [1].

## 2. Sensory TRC pipe Construction

To start the development of a constructional concept the utilized materials are to be determined.

### 2.1. Material Selection

As textile reinforcement a biaxial warp knitted structure is manufactured using alkali resistant (AR)-glass rovings. Two neighboring rovings are replaced by carbon rovings. These carbon rovings resume the sensory function to detect leakage as well as damage of the concrete pipe. Preliminary test were executed to characterize the textile structure. In 4-Point-Bending test according to DIN EN 1170-5 [6] various warp knitted textile structures were analyzed regarding their maximum bending strength. Further comparisons were made with regard to the effect of coating systems. Those tests lead to the conclusion to utilize an open tricot structure, coated with 50 % styrol buthadien rubber (SBR) in water soluble dispersion. This choice is based on the fact that in an open tricot the grid openings are not closed by knitting threads. In addition, the rovings in the open tricot have an oval cross-sectional shape, which is advantageous when penetrated by the coating material and the concrete matrix. The coating is used to increase the internal bond of the filaments in the roving and thus the strength of the structure. Fig. 1 shows the open tricot including the sensory carbon rovings with a coating of 50 % SBR. A fine-grained concrete is used as the matrix to ensure penetration of the small mesh openings of the textile.

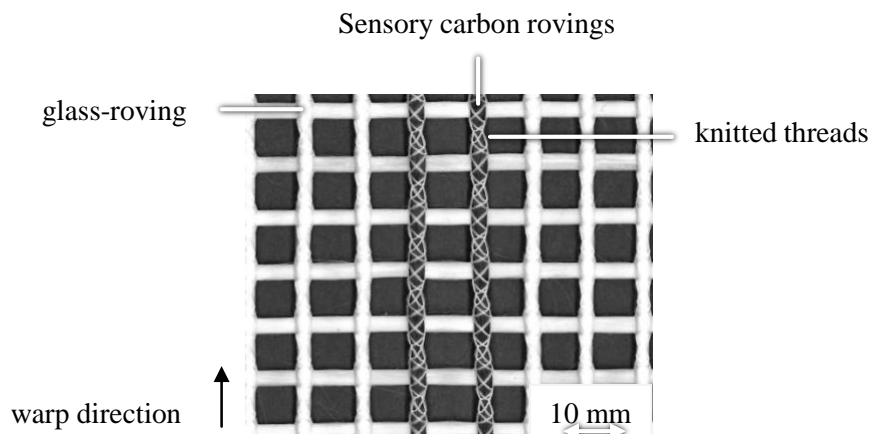


Fig. 1: Open tricot reinforcement structure, two sensory carbon rovings, 50 % SBR coating

### 2.1. Construction concept

Fig. 2 shows a schematic illustration of pursued concept. According to DIN V 1201 [7], a minimum concrete cover of 15 mm inside and 20 mm outside of the steel reinforcement applies to reinforced concrete pipes that remain permanently in the ground. To take into account the advantage of thin-walled construction of TRC structures, a total wall thickness of 25 mm is targeted for TRC pipes. This leads to a distribution of 10 mm inner and 15 mm outer concrete cover.

In the manufacturing process, the textile is bent and coated in a diameter of, in this case, 270 mm. The textile is then positioned in the mold. The mold consists of a base plate and an inner and an outer mold tube. After the textile has been placed, the concrete matrix is prepared and poured into the mold.

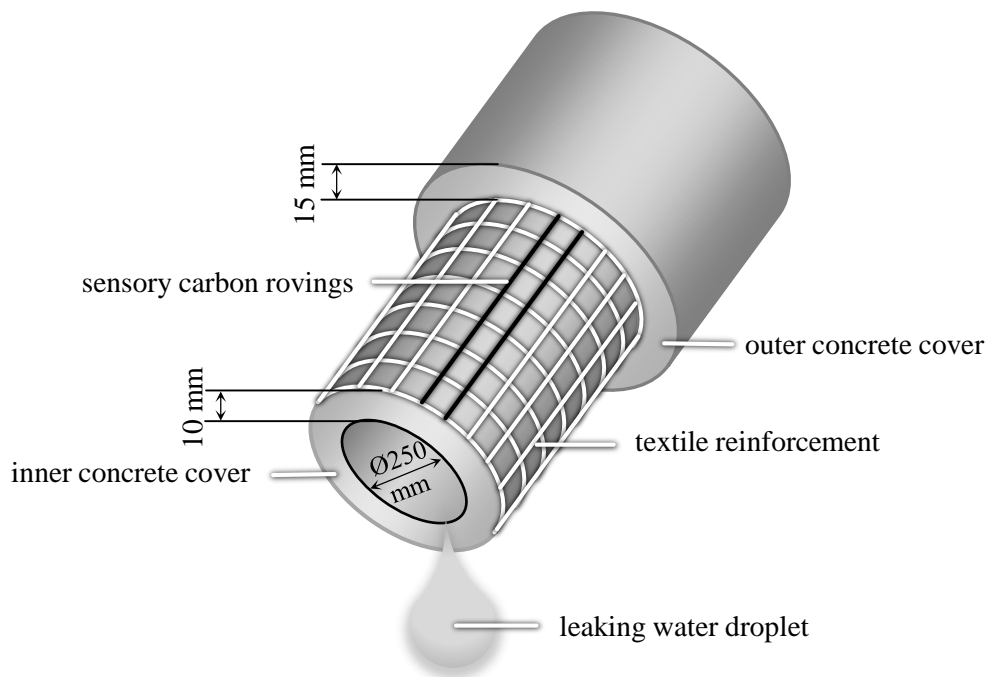


Fig. 2: Schematic illustration of smart TRC pipe

#### 4. Conclusion

This concept has been developed at the Institute fuer Textiltechnik of RWTH Aachen University and will be executed in upcoming studies. Those studies will include an examination of the positioning accuracy and the position retention of the textile during and after the casting process. In addition, soffit pressure tests will be carried out to verify the load-bearing capacity of the TRC pipes. Regarding the production and application, a concept for contacting individual pipe sections, including ensuring positioning accuracy, must be developed. Considerations must also be made as to how a leakage can be located in a one kilometer long pipe network, or how the location can be narrowed down in order to be investigated using conventional methods. Finally, investigations must be carried out to determine the radius in which the carbon rovings are able to detect a leakage. In this way, the arrangement of the rovings along the circumference of the pipe can be concluded.

#### Acknowledgements

We thank the Federal Ministry of Education and Research (BMBF) for the funding of the research project “Smart Pipe” and the Project Management Agency Karlsruhe (PTKA) for the project coordination.

#### References

1. C. Cherif, H. Schorn, H.-B. Horlacher, P. Offermann, “Entwicklung und Erprobung neuer, innovativer Verbundrohrsysteme (Kunststoff-Textilbeton-Verbundsystem) einschließlich ihrer Herstellungstechnologie“ Schlussbericht zum AiF-Forschungsprojekt, 2006, Tu Dresden
2. I. G. Colombo, A. Magri, G. Zani, M. Colombo and M. di Prisco, “Erratum to: Textile Reinforced Concrete: experimental investigation on design parameters“ in *Materials and Structures* , 2013, Vol. 46, pp. 1953-1971
3. T. Quadflieg, Y. Goldfeld, G. Dittel, T. Gries, “New Age Advanced Smart Water Pipe Systems Using Textile Reinforced Concrete“ in *Procedia Manufacturing*, 2018, Vol. 21, pp. 376-383
4. A. Peled, A. Bentur, B. Mabasher, “Textile reinforced Concrete”, CRC Press, 2007, Boca Ranton, Florida, USA
5. Y. Goldfeld, T. Quadflieg, T. Gries, O. Rabinovitch, “Smart textile reinforcement with embedded stainless steel yarns for the detection of wetting and infiltration in TRC structures”, in *Sensors and Actuators A: Physical*, 2016, Vol. 243, pp. 139-150
6. DIN EN 1170-5 Prüfverfahren für Glasfaserbeton, Teil 5: Bestimmung der Biegezugfestigkeit, Vollständige Biegezugprüfung, 1998
7. DIN V 1201 Rohre und Formstücke aus Beton, Stahlfaserbeton und Stahlbeton für Abwasserleitungen und-Kanäle, 2003

# In-process integration of fibre optical sensors for structural condition monitoring of braided composite shaft

Oscar Bareiro<sup>1</sup>, Andreas Preisler<sup>2</sup>, Pascal Drichel<sup>3</sup>, Philippe Ackermann<sup>4</sup>, Kai-Uwe Schröder<sup>1</sup>, Thomas Gries<sup>2</sup>, Georg Jacobs<sup>3</sup>, Robert Schmitt<sup>5</sup>

1 Institut für Textiltechnik, RWTH Aachen University, Otto-Blumenthal-Str. 1, 52074 Aachen, Germany, oscar.bareiro@ita.rwth-aachen.de.

2 Institute of Structural Mechanics and Lightweight Design, RWTH Aachen University, Wullnerstr. 7, 52062 Aachen, Germany

3 Institute for Machine Elements and Systems Engineering, RWTH Aachen University, Schinkelstr. 10, 52062 Aachen, Germany

4 Fraunhofer Institute for Production Technology IPT, Steinbachstr. 17, 52074 Aachen, Germany

5 Laboratory for Machine Tools and Production Engineering, RWTH Aachen University, Campus-Boulevard 30, 52074 Aachen, Germany

## Abstract

Impact damage poses a severe threat for composite structures. Especially barely visible impact damages are a concern since they are not easily detected in service. Structural Health Monitoring (SHM) is a tool to detect and assess such damages online and in service. However, SHM is a complex field of research that requires more than the mere application of sensors to a structure. The current contribution describes an interdisciplinary approach utilizing zero strain direction as structural damage indicator. The fibre optical sensors were integrated within manufacturing of a braided shaft. Drop tower tests were performed to introduce damage. Afterwards a torsional load was applied. During loading, the sensor signal clearly indicated the presence of damage.

**Keywords:** structural health monitoring, braided composite, glass-fibre reinforced plastic, optical fibre sensor, sensor integration, structural damage indicator.

## 1. Introduction

Step by step, lightweight design has evolved to the present day [11]. At first, the general principles and equations of light-weight design were derived. The next step was achieved by the widespread use of the Finite Element Method (FEM) alongside the enormous grow of computational power. The development of high performance materials (e.g. fibre reinforced plastics (FRP)) represents the third step. Nowadays, the major challenge of modern lightweight design is the handling of uncertainties, which might lead to premature damage. In case of metallic structures, fatigue cracks are a concern. If structures made of FRP are considered, internal damages like delamination and matrix cracking represent a severe threat. Such damage might be introduced by manufacturing defects, impacts and/or fatigue. Under compression or shear load, delamination leads to a large drop of stiffness and strength, although the damage might be invisible for the bare eye. In this case, the damage is often referred to as barely visible impact damage (BVID).

In the current state of damage tolerant lightweight design, regular inspections are required to detect damage before they grow to a critical size and thus endanger safe operation of the structure. The accuracy of visual inspections especially in case of small damages can be increased by the use of non-destructive testing (NDT) methods. Classic examples for NDT include ultrasonic testing, radiographic testing and thermography [5]. Those methods are all capable of detecting an internal damage like delamination and might be used to detect BVIDs. However, those methods require either large and heavy equipment or are very time consuming in order to cover a larger surface. Thus, those methods are only capable of a so called off-line monitoring, while the structure is not in service.

A more efficient use of a structure is achieved, if the use of inspections and NDT (off-line monitoring) is reduced to a minimum extend. In this case, potential damage is to be detected in-service (on-line) with integrated monitoring systems. This approach is referred to Structural Health Monitoring (SHM).

### 1.1 Structural Health Monitoring

Structural Health Monitoring (SHM) is the automatic online monitoring of structural integrity during service [11]. Rather simple systems aim to detect the mere presence of damage. A more sophisticated approach localizes, qualifies

and quantifies damage, in order to enable damage assessment. Rytter [13] distinguished between four different levels of diagnosis:

- Level 1: (detection) provides qualitative information of the mere presence of damage within the structure.
- Level 2: (localization) estimates the location of damage.
- Level 3: (assessment) determines the size of the damage as well.
- Level 4: (consequence) evaluates the actual safety of the structure.

With increasing level of diagnosis, the monitoring effort and system complexity rises. Level 1 refers to a relatively simple system, which only triggers an inspection of the structure in case of damage. Level 4 corresponds to a sophisticated SHM system, which is capable of decision making. In this case, the system will assess the damage and evaluate whether the damage is critical or not, including an estimation of residual strength. An additional classification is made according to the scope of the SHM systems [11]:

- Global SHM considers all possible damages of the whole structure. This approach includes accidental and impact damages as well. If a global SHM is needed, usually the first two level of diagnosis are considered, due to the enormous increase of system complexity. Here, data based (statistical) methods like pattern recognition [2] perform well.
- Local SHM focuses the monitoring effort on a local domain. Monitoring of safety-critical parts or fatigue damage is usually referred to local SHM. Here, the scope of the needed SHM is well defined and thus, higher level of diagnosis can be considered. For local SHM and especially if damage assessment is needed, so called physic-based approaches, where the damage is related to its influence on a physical behaviour, perform well.

Usually, different sensor types and measurement techniques are used for the different types of SHM (global and local). The fibre optical sensor (FOS) is one sensor type which is of interest for both type of SHM. FOS are suitable for strain measurements and thus suitable for physic-based approaches. Using FOS with Fibre Bragg Gratings (FBG) [12], strain is measured with high accuracy at a single or several points within the fibre. However, distributed fibre optical sensors using optical frequency domain reflectometry (OFDR) [12] are capable of measuring in continuous manner over length of the fibre. This feature is of interest in particular for global but also for local SHM systems. With a well-designed placement of the OFDR FOS, a large area is covered and monitored. In combination with FRP, integration of the FOS within the production process is possible. Thus, the sensor can be placed within the material instead of applying it on the surface.

Based on structural analysis, so called Structural Damage Indicators (SDI) [11, 4] can be defined. While common damage indicators extract damage features from the measured data, the SDI is introduced by careful consideration of the structural behaviour and the influence of damage in advance of design of the SHM system itself. The monitored signal is not only compared with the signal at the initial stage but with a structure response parameter in the ideal state. Thus, the measurement of the initial state can also be considered as intrinsic quality assurance. This is in particular very efficient, if the ideal state refers to structure response parameter of zero. In that case, the presence of non-zero measurements directly correlates to the presence of damage. Since severe damages will have a significant influence on the structural behaviour regardless environmental changes, SDIs are considered to be reliable and sensitive.

In previous work, efficient strain-based SDIs for a plate in the post-buckling regime [15], for beam and truss structures [11] and for single lap adhesive joints [8, 9] were derived. A comparable approach was shown for a beam in flexural vibration [4]. In this contribution, a braided composite shaft under torsional load is considered, utilizing the so called zero-strain trajectories, proposed by Schagerl et al. [14]. The principle idea for the application of zero-strain trajectories on a braided shaft was already described in previous work [10]. In the current contribution, the approach is validated within experiments.

## 1.2 Braiding process

The braiding technology has been gaining importance for composite preform manufacturing. It can produce components with complex hollow geometries and high load bearing capacities for different applications. A common technique used for manufacturing braided composites is the circular braiding process with radial braiding machines (see Fig. 1). In the braiding process, the deposition of off-axis and standing axial yarns is realized by two sets of counter rotating circumferential bobbins moving in a sinusoidal motion around stationary bobbins. The fibre yarns are

pushed through the braiding ring and are deposited onto the surface of the mandrel forming the textile preform. Parameters of the process include: number of active bobbins, braid take up and circumferential speeds, types of yarns used, dimensions of the braiding machine and braiding mandrel; these parameters determine the final preform shape and yarn architecture.

The fibre architecture along the mandrel axis can be modified by robotically guiding a mandrel through the centre of the machine with a defined speed. The final braid pattern is the result of the interaction of yarns along the circumference of the machine, yarn configuration, mandrel geometry and robot-controlled path of the mandrel [6].



Fig. 1: Radial braiding machine with robotic arm which guides the mandrel.

## 2. Measurement concept for braided composite shafts

Within this paper, the approach of using SDI is applied on a braided composite shaft. The shaft has a constant diameter and thickness, using three layers of glass fibre reinforced plastic (GFRP) during the manufacturing process. Compared to regular aluminium shafts, this structure is not prone to fatigue damages. However, impact damages are a concern. Thus, a monitoring system is needed which covers the whole surface of the braided GFRP shaft. Using OFDR FOS, a large area is monitored while strain as local quantity is measured. Thus, a global monitoring system based on a local quantity can be applied with reasonable effort.

The first step for applying SDI is to analyse the structural behaviour of the undamaged and the damaged shaft in order to get a complete understanding of the load carrying behaviour and the influence of potential damages: The shaft is loaded by a torsional load, considering a fixed-fixed boundary condition. Thus, the Poynting effect [7] can be neglected and pure shear deformation is present in case of an undamaged shaft. Fig. 2(Left and Centre) illustrates the stress state for pure shear for a 2D element. Considering a rotation of  $45^\circ$ , shear stress is changed to tensional stress in  $x_1$  direction and compressive stress in  $x_2$  direction. They are referred to as the principal stresses.

If impact damage is present, the stiffness is locally reduced and thus, shear stresses are redistributed within a certain area. Fig. 2(Right) shows the direction of principal stresses for the undamaged state (left) and in case of damage (right). Here, the principal direction is rotated and significant stress in longitudinal direction is present as well. This effect is utilized as SDI. In the ideal state, there is no strain along the longitudinal direction of the shaft. Thus, this direction is referred to as the zero-strain direction. Only if damage occurs, strain is present in this direction. This leads to a very powerful SDI, where the mere presence of a non-zero value refers to damage. If FOS with OFDR are used, longitudinal strain over the whole length of the shaft is monitored. Damage is detected by a distinct deviation from the expected zero-strain. Since OFDR provides strain measurements at each position of the fibre, the damage is easily localized. Thus, the use of the FOS with OFDR in longitudinal direction already provides a level 2 monitoring according to Rytter. However, the amplitude of the measured strain is dependent on the severity of damage, the circumferential distance to the damage and also on the load level.

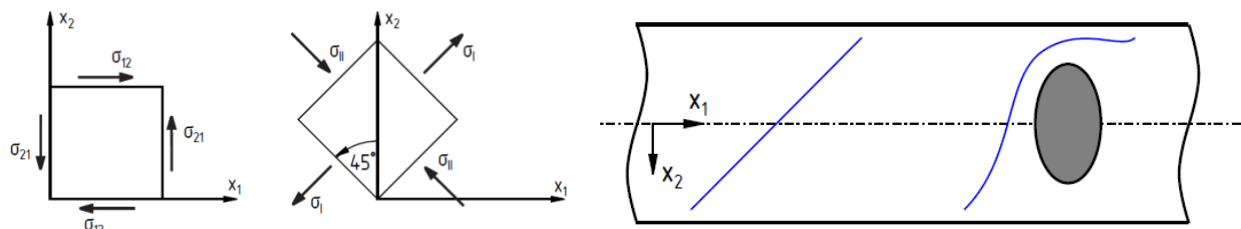


Fig. 2: (Left) Pure shear illustrated for a 2D element and (Centre) its principal stresses. (Right) Direction of principal stresses for torsion loaded shaft in the undamaged case (left) and the damaged case (Right) [10].

Assuming that the load level is known, two FOS positions are needed within the area which is affected by the damage to triangulate and assess the damage, as explained in previous work for strain gauges [11]. Finite Element Method (FEM) can be used to correlate the severity of damage and its distance to the SDI. Thus, numerical models provide the basis for damage assessment.

### 3. Test setup

For validation of the proposed SDI, GFRP shafts are manufactured using the braiding process. During manufacturing, the FOS are already integrated within the textile preforms. Afterwards, the specimens are impacted during drop tower tests. Then, static torsion is applied to the damaged shafts in order to validate the monitoring approach.

#### 3.1 Manufacturing process and sensor integration

The textile preforms were braided using a radial braiding machine (Herzog RF 1/144 – 100) onto foam core bodies with 65 mm diameter of the material ROHACELL 110 IGF. The foam core was fitted with aluminium sleeves on both end faces. The sleeves were later used to couple the shaft to the testing machine for torsional testing. Three layers of glass fibre were braided onto the mandrel to obtain a wall thickness of 1.5 mm. The braiding machine settings were adjusted to generate a braiding angle of  $\pm 45^\circ$  (see Fig. 3(Left)). FOS were introduced as longitudinal yarns so that they run straight and parallel with respect to the braiding direction (see Fig. 3(Centre)). In total, four FOS were integrated separated by an angular distance of  $15^\circ$  with respect to each other. In real application, the FOS should be evenly distributed over the circumference. Here, the FOS were focused close to the area where damage was later introduced by impact. Afterwards, the braided composite was consolidated in a Resin Transfer Moulding (RTM) process using epoxy resin. A special RTM moulding dye was designed and constructed to protect the FOS from damage during the curing process. The RTM moulding dye consisted in two aluminium half shells which surrounded the mandrel and sleeves. The FOS were led out through a quarter-circle opening at the end plate of the moulding dye. A strong bonding between the driving shaft and the sleeves was created during the resin curing; this is required to transmit the applied torque of 300 Nm to the shaft during torsional tests. In total four braided shafts with integrated sensors were produced. Fig. 3(Right) shows one half shell of the moulding dye with a finished GFRP shaft. The red lines were added with a pen to mark FOS positions.

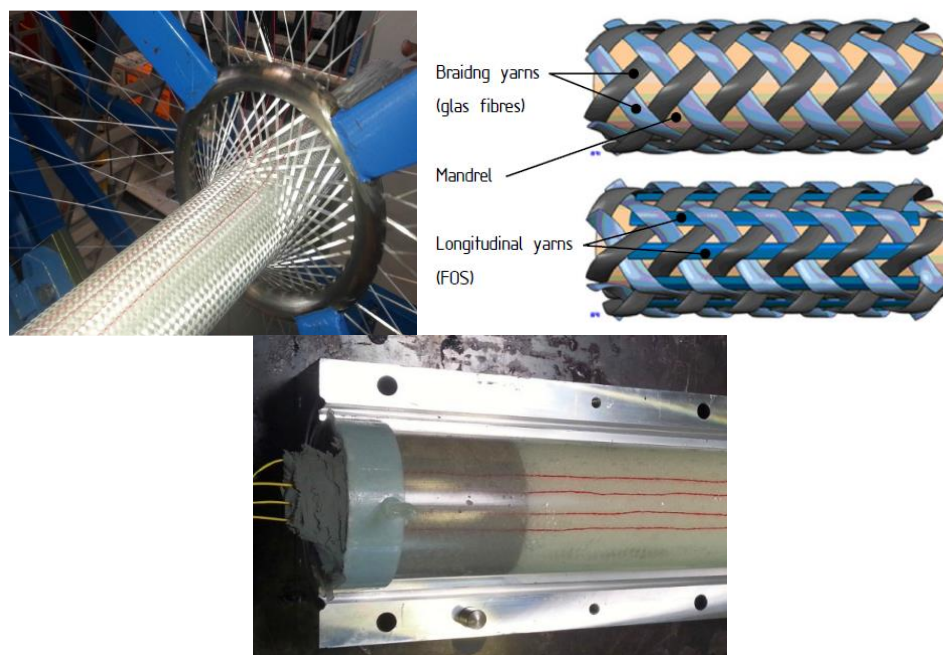


Fig. 3: (Left) Photographic image of the braided preform with integrated. (Centre) Schematic representation of the textile preform on the mandrel. The braiding yarns, glass fibres, and also the longitudinal yarns (FOS) are indicated FOS.

(Right) Aluminium half-shell of the moulding dye with a GFRP shaft after manufacturing.

It should be mentioned, that only 50 % of all FOS were functional at this stage. It is unknown, whether the FOS were damaged during the manufacturing process or afterwards during handling or transportation of the specimens. Due to the small diameter of a single FOS, the free part of the FOS is very vulnerable to damage during handling.

### 3.2 Damage introduction

After manufacturing, damage was introduced into the braided shafts within drop tower tests. All four manufactured shafts

were impacted. The impact tests were performed with an impact energy of 10 J. A square aluminium profile with an angle of 45° and a total mass of 3.26 kg was used as impactor. Drop height was 0.32 m. Two shafts were impacted twice, while the other two were impacted once. In Fig. 4(Left) the position of the impacts are shown. Fig. 4(Centre) shows a photograph of the drop tower tests immediately before impact. The position of the fibre optical sensors is marked with red lines. The black crosses refer to positions of impacts.

All drop tower tests produced a comparable damage pattern. After the impact, a clouded surface developed which can be described as an elliptical or peanut-shaped surface (see Fig. 4(Right)). Within this clouded surface matrix damage and delamination is present. Fibre breakage is also expected near the impact point. Tab. 1 summarizes the visible extend of all impact damages. Here,  $d_2$  refers to the length within longitudinal direction of the shaft and  $d_1$  refers to the length in circumferential direction.

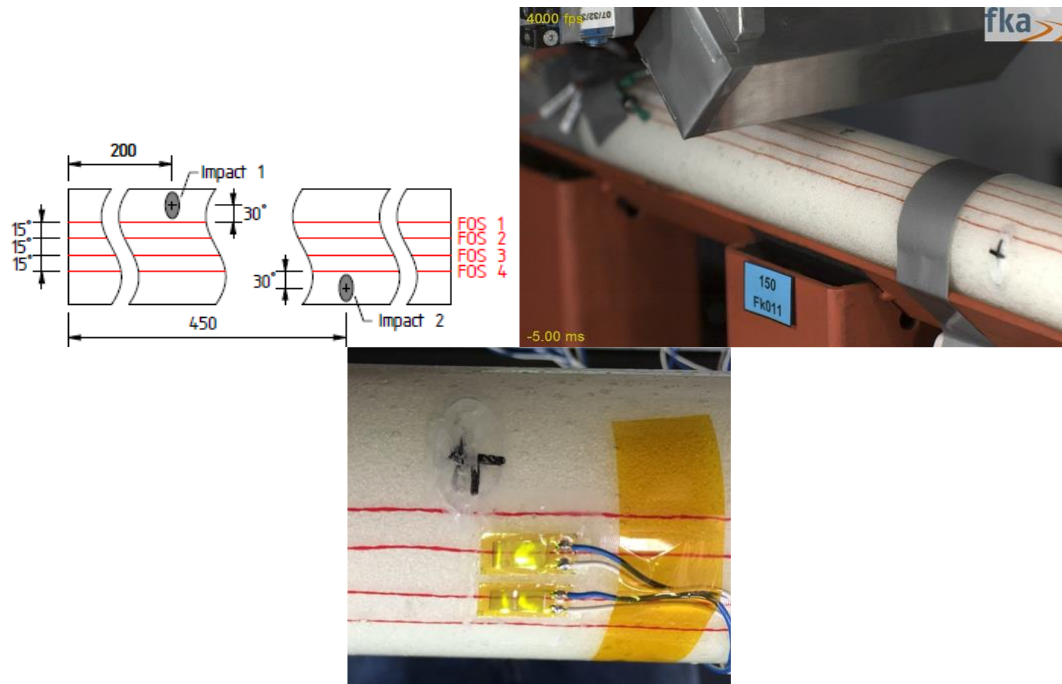


Fig. 4: (Left) Sketch of the position of the impact and the FOS (measurements in circumferential direction are given in degrees). (Centre) Setup of the drop tower tests. (Right) Impact damage after drop tower test.

Tab. 1: Visible extend of the impact damages ( $d_2$  refers to the longitudinal direction and  $d_1$  refers to the circumferential direction).

Damage No.	$d_1$	$d_2$
Shaft 1, impact 1	20 mm	30 mm
Shaft 1, impact 2	15 mm	30 mm
Shaft 2, impact 1	15 mm	35 mm
Shaft 3, impact 1	18 mm	32 mm
Shaft 4, impact 1	15 mm	30 mm
Shaft 4, impact 2	20 mm	35 mm
Mean value	17 mm	32 mm

### 3.3 Torsional test

After the damage introduction within drop tower test, torsional tests were performed. Due to a large amount of damaged FOS, only shaft 1 and shaft 4 are considered at this point. The pre-damaged shafts were applied to a torsional test bench with a nominal torque of 4000 Nm. Torque and torsional angle were measured and acquired via an MTS data acquisition system. The strain of the FOS was logged with a separate POLYTEC data acquisition system. Fig. 5(Left) shows the setup of the torque test. The shaft was mounted on the test bench with the help of several adapting units. A sliding hub was installed to avoid mechanical impacts from the hydraulic system which might occur during the start-up of the test ramp. The static torsional tests were conducted by applying torque with a step size of 50 Nm between a range of 0 Nm to 300 Nm and held constant for a timespan of approximately 200 s (see Fig. 5(Right)). During that time, measurements of the FOS and two reference strain gauges were performed.

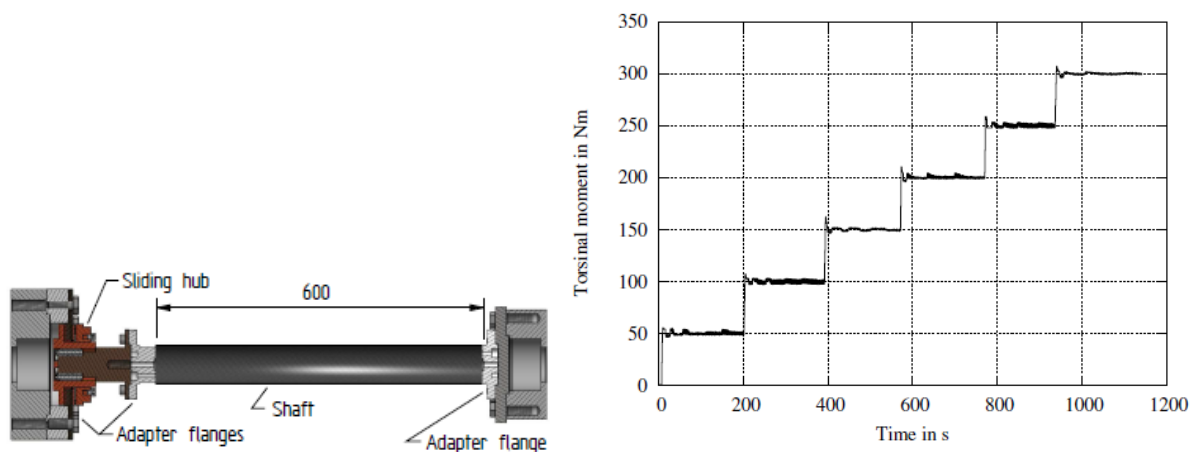


Fig. 5: (Left) Sectional view of the specimen at the test bench. (Right) Applied torque over time.

#### 4. Test results

During the static torque test, all four FOS were evaluated at each load level (50 Nm, 100 Nm, . . . , 300 Nm). However, only FOS 3 of shaft 1 provided a meaningful reading. All other sensors were damaged during the manufacturing process, transportation, handling or impact. Thus, this section focuses on shaft 1.

For comparison, strain gauges were applied at the position of FOS 2 and FOS 3 at the position 455 mm. Fig. 6(Left) shows the results of the strain gauges. In case of an undamaged structure, both strain gauges would measure zero strain. Due to impact damage 2, a certain amount of strain is redistributed in a local regime. The strain gauge at the 3rd FOS is closer to impact 2 and thus measures larger amount of strain. For higher loads (above 200 Nm, after approx. 600 s), a time-dependent behaviour was present and strain increases further. However, this viscoelastic behaviour was not further investigated.

Fig. 6(Right) shows the reading of FOS 3 for all load levels. The first and last 80 mm were not considered, since the reading in that area was influenced by the aluminium sleeves. The characteristic shape of strain distribution due to damage can be seen at three different positions. The clearest signal is at the position 445 mm. This position refers to impact 2. Here, is a distinct minimum present which is followed by a strongly pronounced maximum. The measured strain almost reaches 200  $\mu\text{m}/\text{m}$  in case of a torsional load of 300 Nm. Thus it is concluded, that the impact is above and rather close to the FOS. At the position 200 mm (impact 1) a small maximum is followed by a pronounced minimum. In this case, the damage is below the FOS. The difference between both peaks is smaller, although impact energy was identical during all impacts. This is due to the increased distance of the damage to the FOS. Surprisingly, a third characteristic deviation is found at a position of 320 mm. In this case, no impact damage is present. However, a strain gauge was applied to this position and the surface was slightly damaged during the surface treatment (grinding). The deviation in this case is about 50  $\mu\text{m}/\text{m}$ .

As described, both impact damages and even the minor surface damage due to grinding are clearly detected by FOS 3. In addition, a clear deviation is present within the first 200 mm. The expected zero-strain is not measured within that area. There is also a mismatch of the amplitudes from minimum and maximum at impact 1.

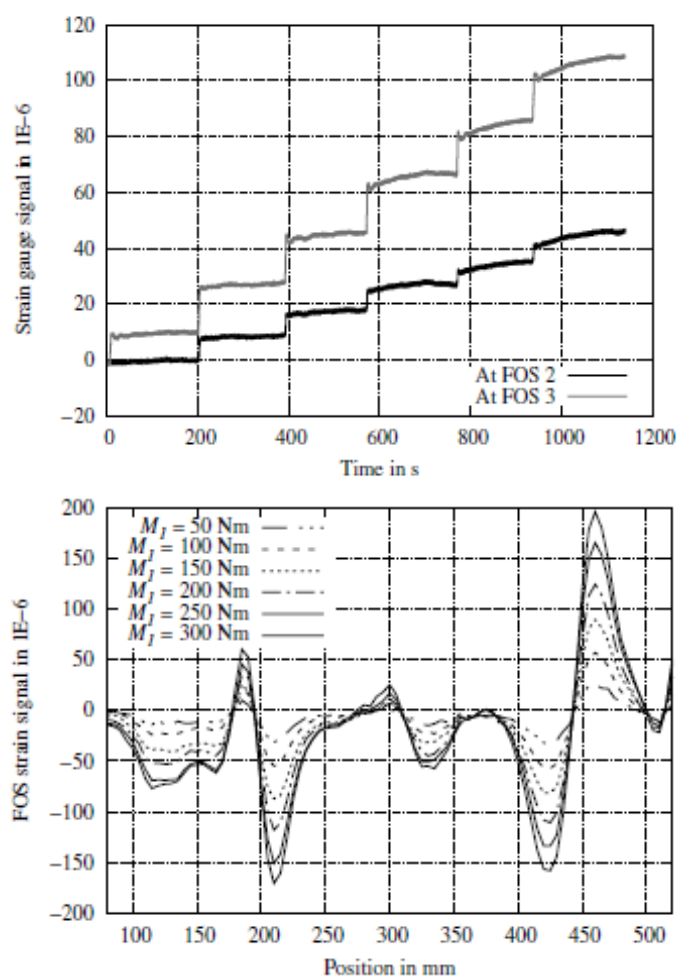


Fig. 6: (Left) Results of the strain gauges at the position 455 mm. (Right) Strain reading of FOS 3 for all load levels. M1 refers to the applied torsional moment.

## 5. Conclusion

Within this contribution, zero-strain trajectories were used as SDI for a torsional loaded braided shaft. FOS with OFDR were used to measure the SDI and to detect impact damage. Already during the braiding process, FOS were integrated as longitudinal yarns. Afterwards, drop tower tests damaged the braided shafts, which then were tested within torsional tests to detect the damage using the FOS. During torsional tests, the FOS achieved a clear damage signal. All damages, even a non-expected superficial damage due to grinding, were detected. However, some noise, leading to a non-zero signal, was present. It is assumed, that slight sensor misalignments of approximately 1 caused the measurement noise, leading to the non-zero signal. For a rough level 2 diagnosis according to Rytter, one FOS is needed within the area which is affected by the damage. If full damage assessment is needed, it is assumed that two FOS are able to distinguish between a close, small damage and a more severe but distant damage. Considering, that damage within  $45^\circ$  circumferential distance was easily detected, it is concluded that four evenly spaced FOS positions are needed to assess all potential impact damages. However, only 50 % of all FOS survived manufacturing process, handling and transport. After the drop tower test and additional handling and transport, only one FOS provided a signal over the whole length of the braided shaft. Thus, protection of the sensors, especially at the position where they leave the material, is a concern.

## Acknowledgements

The authors like to express their appreciation to all partners of the smartSHM group at the RWTH Aachen and Fraunhofer for their valuable and constructive suggestions. In particular, the authors are thankful for the active contribution of the Institute of Automotive Engineering for the drop tower tests, the Welding and Joining Institute for manufacturing of the adapter flanges for the torsional tests and Georg Merzenich (enjoy Innovation!).

## References

1. Barre de Saint-Venant, A.J.: Memoire sur la torsion des prismes. *Mem. Divers Savants* 14, 233–560 (1855)
2. Farrar, C.R., Worden, K.: An introduction to structural health monitoring. *Philosophical transactions. Series A, Mathematical, physical, and engineering sciences* 365(1851), 303–315 (2007). DOI 10.1098/rsta.2006.1928
3. Gay, D., Mann, N.: *Composites materials: Design and applications*, 3 edn. CRC Press (2002)
4. Huang, T., Chaves-Vargas, M., Yang, J., Schröder, K.U.: A baseline-free structural damage indicator based on node displacement of structural mode shapes. *Journal of Sound and Vibration* 433, 366–384 (2018)
5. Konstantopoulos, S., Fauster, E., Schledjewski, R.: Monitoring the production of frp composites: A review of in-line sensing methods. *eXPRESS Polymer Letters* 8(11), 823–840 (2014). DOI 10.3144/expresspolymlett.2014.84
6. Pickett, A.K., Sirtautas, J., Erber, A.: Braiding simulation and prediction of mechanical properties. *Applied Composite Materials* 16(6), 345–364 (2009). DOI 10.1007/s10443-009-9102-x
7. Poynting, J.H.: On pressure perpendicular to the shear planes in finite pure shears, and on the lengthening of loaded wires when twisted. *Proceedings of the Royal Society A: Mathematical, Physical and Engineering Sciences* 82(557), 546–559 (1909). DOI 10.1098/rspa.1909.0059
8. Preisler, A., Sadeghi, Z., Adomeit, A., Schröder, K.U.: Damage assessment in adhesively bonded structures by using smartshm. In: F.K. Chang (ed.) *System Reliability for Verification and Implementation*. DEStech Publications (2015). DOI 10.12783/SHM2015/27
9. Preisler, A., Sadeghi, Z., Schröder, K.U.: Monitoring of fatigue damages in adhesively bonded joints. In: J.J. Remmers, A. Turon (eds.) *Proceedings of the sixth ECCOMAS Thematic Conference on the Mechanical Response of Composites*, pp. 188–199 (2017)
10. Preisler, A., Schroder, K.U.: Ein interdisziplinärer ansatz zur intelligenten fvk welle. In: M. Wiedemann, T. Melz (eds.) *Symposium fur Smarte Strukturen und Systeme*, pp. 15–27. Shaker Verlag (2017)
11. Preisler, A., Schröder, K.U., Schagerl, M.: Intrinsic damage assessment of beam structures based on structural damage indicators. *American Journal of Engineering Research* 7(6), 56–70 (2018)
12. Ramakrishnan, M., Rajan, G., Semenova, Y., Farrell, G.: Overview of fiber optic sensor technologies for strain/temperature sensing applications in composite materials. *Sensors* 16(1) (2016). DOI 10.3390/s16010099
13. Rytter, A.: *Vibration based inspection of civil engineering structures*. Phd thesis, Aalborg University, Aalborg, Denmark (1993)
14. Schagerl, M., Viechtbauer, C., Schaberger, M.: Optimal placement of fiber optical sensors along zero-strain trajectories to detect damages in thin-walled structures with highest sensitivity. In: F.K. Chang (ed.) *System Reliability for Verification and Implementation*, vol. 1, pp. 1096–1103. DEStech Publications (2015)
14. Viechtbauer, C., Schagerl, M., Schroder, K.U.: Validation of structural parameters as damage indicators for monitoring plates in the post buckling regime. In: V. Le Cam, L. Mevel, F. Schoefs (eds.) *EWSHM - 7th European Workshop on Structural Health Monitoring* (2014)

# Control of Vibration Suppression of Planar Structures Using Actuation by Clusters of Piezopatches

Jiří Volech<sup>1</sup>, Zbyněk Šika<sup>1</sup>, Filip Svoboda<sup>2</sup>, Martin Hromčík<sup>2</sup>, Jan Zavřel<sup>1</sup>, Jindřich Karlíček<sup>1</sup>  
<sup>1</sup> Czech Technical University in Prague, Department of Mechanics, Biomechanics and Mechatronics, Prague, Czech Republic, [Jiri.Volech@fs.cvut.cz](mailto:Jiri.Volech@fs.cvut.cz), [Zbynek.Sika@fs.cvut.cz](mailto:Zbynek.Sika@fs.cvut.cz)  
<sup>2</sup> Czech Technical University in Prague, Department of Control Engineering, Prague, Czech Republic,

## Abstract

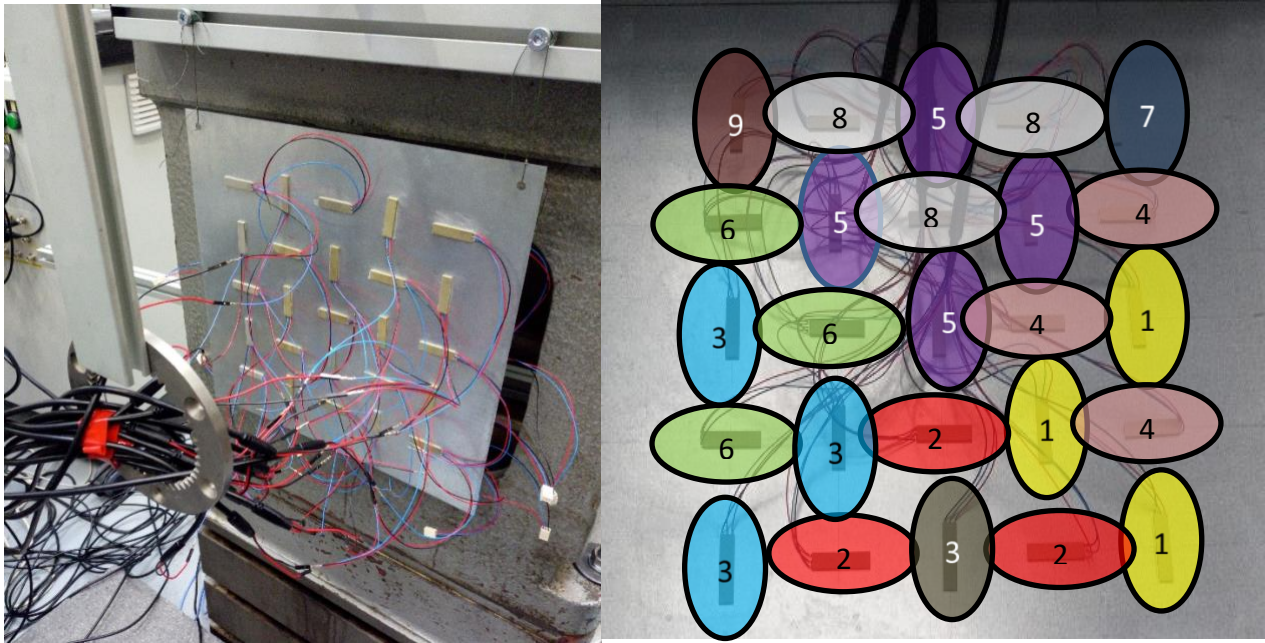
“Intelligent materials” are nowadays the perspective subject of research. Thanks to piezo material price developments, one type of this material could be the common material with heavily distributed piezo elements. Such material can still have lightness, flexibility and approximately other aspects of the original material, but with the added energy these properties may be partially modified. The paper deals with optimization and control of vibration suppression of the planar flexible systems equipped by regular and dense matrix of multiple sensors and actuators. The proposed concept consists from the steel cantilever beam with three piezoelectric patches. FEM model of such concept was created to test its accuracy compared to reality. A detailed description of this problem could be seen in [1]. On this model, the H-infinity controller was designed and subsequently tested on the real experiment with promising results. Based on these results, the model was extended to a square plate with distributed piezo patches in the 5x5 grid. The results from decentralized control law synthesized by the h-infinity will be presented. Results are promising, but such a heavily distributed grid still leads to demands on the initial expense. The actuators and sensors are not that big problem, the problem occurs with the amplifiers needed to power individual piezo elements. In order of further savings, four more concepts were proposed and will be presented. There are formed several groups “clusters” of piezo patches which are powered with a single amplifier and single control voltage. These clusters are then subject of an analysis based on total energy loss using the Hankel matrix and controllability criteria. The results showed that the system can be controlled with minimal energy loss for each mode with only nine amplifiers and nine different inputs voltages. That leads to saving the 16 amplifiers and open the possibilities of further improvements.

**Keywords:** distributed actuators; distributed sensors; distributed control; vibration suppression, model reduction

## 1. Introduction

Smart material capable of vibration suppression or shape change is nowadays a very active field of research. The main advantage of using smart materials and structures are their potential to bring the new features in the standard application and technologies. This technology needs to be controlled in the right way and the suitable control strategy is distributed control law. With this control strategy the measured data are collected and then distributed to actuators using H-infinity control synthesis. This principle can be applied to various systems [4]. To successfully apply the vibration suppression or the shape change of the researched system the precise FEM model with many degrees of freedom is needed to be obtained [5][6]. Such a model is very large and unsuitable for control strategy. Therefore, model order reduction is applied [7][6] to give accurate enough yet tractable models for optimal actuators and sensors placement [8][9][10]. Second approach is for already existing prototypes. It using experimental identification to obtain mathematical model from measured data [11]. With such mathematical model the proper control synthesis can be designed to reach desirable outcome. In our case its vibration suppression of the plate with heavily distributed grid of piezopatches

a) experimental demonstrator                      b) piezo „clusters“  
Fig. 1 a).



a) experimental demonstrator      b) piezo „clusters“

Fig. 1. Experimental demonstrator

## 2. Piezo clusters

Fully actuated system is demanding for control strategy and initial cost due to fact, that each piezopatch demands one amplifier. Merging piezopatches to groups “clusters” is proposed for simplification of the control law and saving amplifiers Fig. 1 b).

This is achievable using gramians of controllability and observability in stable algebraic Lyapunov form

$$\begin{aligned} \mathbf{A}\mathbf{W}_c + \mathbf{W}_c\mathbf{A}^T + \mathbf{B}\mathbf{B}^T &= \mathbf{0} \\ \mathbf{A}^T\mathbf{W}_o + \mathbf{W}_o\mathbf{A} + \mathbf{C}^T\mathbf{C} &= \mathbf{0}. \end{aligned} \quad (1)$$

For stable  $\mathbf{A}$ , the obtained grammians  $\mathbf{W}_c$  and  $\mathbf{W}_o$  are positive definite and for our case even diagonal. This results can be transformed into balanced representation using transformational matrix  $\mathbf{R}$  obtain via Hankel matrix  $\mathbf{H}$  which can be expressed as

$$\mathbf{H} = \mathbf{Q}\mathbf{P} \quad (2)$$

Where  $\mathbf{P}$ ,  $\mathbf{Q}$  are obtain from the decomposition of the controllability and observability grammians, respectively

$$\begin{aligned} \mathbf{W}_c &= \mathbf{P}\mathbf{P}^T \\ \mathbf{W}_o &= \mathbf{Q}\mathbf{Q}^T. \end{aligned} \quad (3)$$

Then decomposing the Hankel matrix using SVD decomposition

$$\mathbf{H} = \mathbf{V}\mathbf{\Gamma}\mathbf{U}^T, \quad (4)$$

can be expressed the transformational matrix  $\mathbf{R}$  as follows, see [2]

$$\mathbf{R} = \mathbf{P}\mathbf{U}\mathbf{\Gamma}^{-1/2}. \quad (5)$$

And its inversion as

$$\mathbf{R}^{-1} = \mathbf{\Gamma}^{-1/2}\mathbf{V}^T\mathbf{Q}. \quad (6)$$

Using above equations, the  $(\mathbf{A}\mathbf{b}, \mathbf{B}\mathbf{b}, \mathbf{C}\mathbf{b})$  matrices of the new balanced state-space representation can be expressed as

$$\begin{aligned} \mathbf{A}\mathbf{b} &= \mathbf{R}^{-1}\mathbf{A}\mathbf{R} \\ \mathbf{B}\mathbf{b} &= \mathbf{R}^{-1} \end{aligned} \quad (7)$$



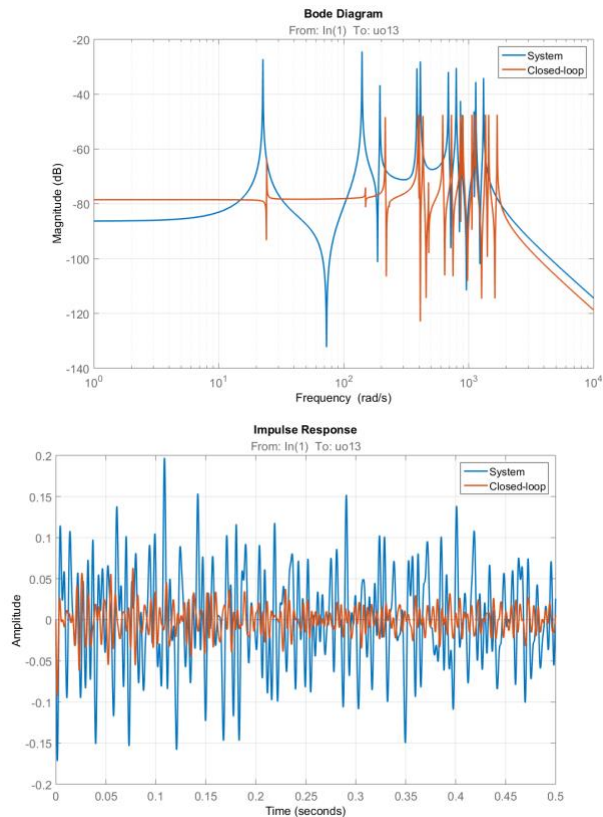


Fig. 3. Bode diagram and impulse response for the decentralized feedback, relaxed gains

Subsequently, the constraint on equal control gains for all nodes was relaxed for both cases studied so far (decentralized and distributed, respectively). The first case then reads  $k_i$ ,  $i = 1, 2, \dots, 25$  could be now different proportional controllers. With this additional “degree of freedom”, this decentralized control law is able to suppress all system resonant frequencies which is clearly visible in the Bode diagram and impulse response (Fig. 3 and **Error! Reference source not found.**). However, some frequency peaks are shifted significantly.

#### 4. Conclusion

The real demonstrator of smart material capable of shape change and vibration suppression was presented. It consists of the plate with heavily distributed grid of piezo patches. For this demonstrator the H infinity control synthesis was proposed for decentralized and distributed cases to minimize impulse response capable to suppress all system resonant frequency. In addition, a possible saving of initial costs was discussed. Using controllability parameter in balanced form via Hankel’s singular values can be reduced 16 amplifiers with minimal loss of energy for each mode.

#### Acknowledgements

The work has been supported by the Czech Science Foundation project Mechatronic structures with heavily distributed actuators and sensors, 16-21961S.

#### References

1. J. Karlíček, Z. Šika, J. Volech, F. Svoboda and M. Hromčík, “Vibration suppression of cantilever beam using collocated piezoelectric,” Bulletin of Applied Mechanics, vol. 13, no. 42, pp. 1-6, 2017.
2. A. Preumont, Mechatronics. Dynamics of Electromechanical and Piezoelectric Systems, Springer, 2006

3. Z. Šika, M. Hromčík, F. Svoboda, J. Volech, J. Zavřel J. Karlíček, Decentralized and distributed MIMO H-infinity robust control of vibration suppression of planar structures In: Proceedings of ISMA2018, International Conference on Noise and Vibration Engineering, including USD2018, (paper ID 588) Leuven: Katholieke Universiteit, 2018,
4. N. Chopra and M. Spong, "Passivity-based control of multi-agent systems," in *Advances in robot control*, Berlin Heidelberg, Springer, 2006.
5. R. R. Craig, "Coupling of Substructures for Dynamic Analyses: An Overview," *American Institute of Aeronautics and Astronautics*, pp. 1573-1593, 2000.
6. M. Kozek, A. Schirrer and (Eds.), *Modeling and Control for a Blended Wing Body Aircraft*, Springer,, 2015.
7. W. Gawronski, *Advanced Structural Dynamics and Active Control of Structures*, New York: Springer-Verlag New York, 2004.
8. T. Haniš and M. Hromčík, "Optimal sensors placement and spillover suppression," *Mech. Syst. Mech. Syst.*, vol. 28, pp. 367-378, 2012.
9. W. Liu, Z. Hou and A. A. Demetriou, "A computational scheme for the optimal sensor/actuator placement of flexible structures using spatial H2 measures," *Mech. Syst. Signal Process*, vol. 20, p. 881–895, 2006.
10. T. Haniš, *Active control for high capacity flexible aircraft*, PhD dissertation, Czech Technical University in Prague, 2012.
11. P. Verboven, *Frequency-domain system identification for modal analysis*, Ph. D. Thesis, Mechanical Engineering Department (WERK), Brussels: Vrije Universiteit Brussel, 2002.

# Distributed control for a morphing wing with a macro fiber composite actuator

Filip Svoboda<sup>1</sup>, Martin Hromčík<sup>1</sup>

<sup>1</sup> Czech Technical University in Prague, FEE, Department of Control Engineering, Prague, Czech Republic

## Abstract

This work offers a new look at the morphing wing control, where the complex dynamical model is represented as a set of interconnected virtual agents and the distributed control paradigms are used. The background theme of this work is the most important of all aeroelastic phenomena causing unstable self-excited vibrations of aeroelastic structures like wings or ailerons. This instability called flutter occurs above the critical (flutter) speed where at least one of the modes is no longer damped. Aeroelasticity is relevant for the design of various structures including bridges, wind turbines, helicopter blades, and similar. This work considers specifically the flexible wing flutter.

**Keywords:** morphing wing, aeroelasticity, flutter, macro fiber composite, distributed control

## 1. Introduction

Flutter can take various forms involving different interacting modes and often leads to catastrophic structural failure. Reduction of structural weight to maximize efficiency and agility for modern aircraft also reduces stiffness and thereby increases the likelihood of flutter. A solution to this problem without structural modifications is active control. The general principle of active suppression approach is that available information is processed about unwanted movements of flexible parts which must be damped. Typically, accelerations at a few points on a wing are measured, and control commands for dedicated aerodynamic surfaces are generated. Active flutter suppression systems become even more important with the new generation of light-weight materials and structures.

In the last 20 years, recent developments in SMART materials helped to examine a new concept of morphing wings [1]. This new promising technology works with the idea of changing the wing shape enabling a mission-adaptive performance [2]. Current conventional wings are usually designed for either a single cruise flight condition or by using a weighted combination of multiple flight conditions, and they are thus not optimal for a wide range of flight modes. Continuous variable wing geometry has significant efficiency, can minimize drag, and it is silent compared to wings with conventional flaps with gaps producing a considerable noise source. Moreover, smart materials are removing energy conversions such as electrical to mechanical to hydraulic forces, reduces the number of individual parts and thus reduce the probability of failure.

Macro-Fiber Composite (MFC) has been used as an actuator for the morphing wing segment model presented in this work. These new aircraft actuation possibilities also motivate novel approaches to control design of active damping and active flutter suppression systems [3]. Especially interesting for this purpose are the distributed and cooperative control concepts dealing with the problem of controlling a multi-agent system, where multiple dynamic local entities share information to accomplish a common global goal.

## 2. Aeroelastic morphing wing model

Dynamic aeroelasticity result from the interaction of three types of force, inertia force, elastic force, and aerodynamic force. This interaction is ensured by a model with a structural part modeled using Finite Element Methods and the aerodynamic part. The equation of motion for the entire system is given in (1), where  $M$ ,  $C$ ,  $K$  are the wing mass, damping and stiffness matrices composed of element matrices and structure shown in the Fig. 2.  $Q$  is a generalized force vector with aerodynamic forces [3]. In this paper, we represent the model as a set of dynamics mutually interconnected with their neighbors. In other words, we have several predefined agents with a given network as shown in Figure 1. Each node  $n_j$ ;  $j = 1, 2, \dots, i$ , represents a particular wing segment in the wingspan, where the airfoil shaping changes local forces on the wing.

$$M\ddot{x} + C\dot{x} + Kx = Q \tag{1}$$

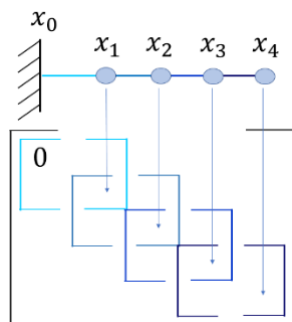


Fig. 2: M, C, K Matrices structures with element matrices.

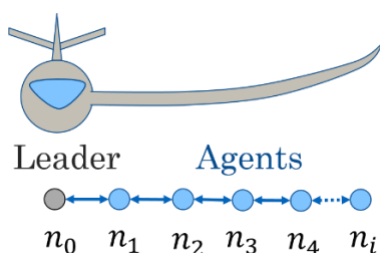


Fig. 3: The dynamics of a morphing wing divided into several wing segments represented as a group of agents.

### 3. Distributed control

We formulate flutter suppression task as state synchronization of agents in a new artificial network, where information can propagate faster and thus speed up the system response. Example can be a connection between the last node (tip of the wing) and the fuselage. It realizes virtual clamping between the fuselage and this node and contributes to system stability. Agent's states synchronization is done by cooperative LQR [3], with input to segment with index  $i$  in equation (2), where  $c$  is a scalar coupling gain,  $K$  is a control gain matrix and  $\epsilon_i$  is neighbourhood synchronization error. This synchronization error (3) depends on adjacency matrix  $A = [a_{ij}]$  and pinning matrix  $G = \text{diag}(g_i)$ .

$$u_i = cK\epsilon_i \quad (2)$$

$$\epsilon_i = \sum_{j \in N_i} a_{ij}(x_j - x_i) + g_i(x_0 - x_i) \quad (3)$$

Distributed control results for the studied case of morphing wing are not yet developed. However, as the related work on heavily distributed active damping for simple mechanical structures suggests, potential robust and efficient performance can be anticipated.

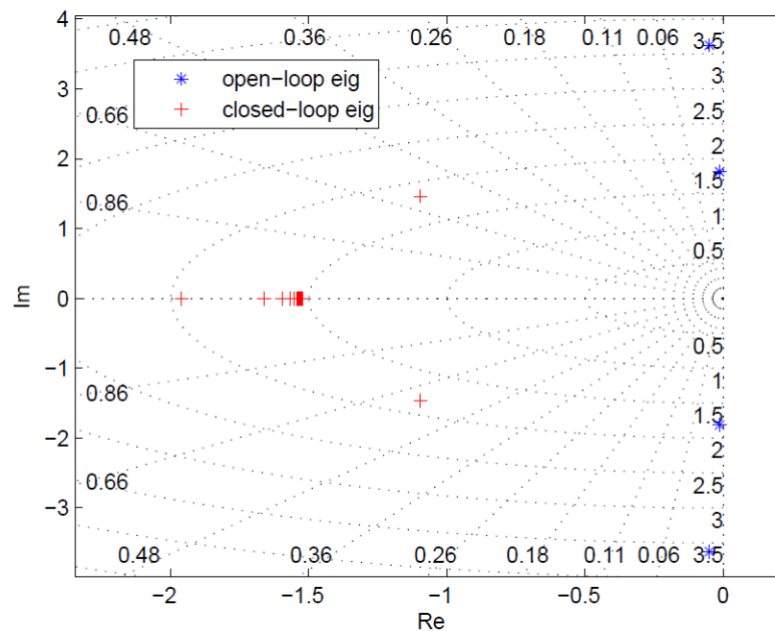


Fig. 1: Root locus of dominant modes - decentralized active damping, adopted from [4].

To prove this assumption for the more complex case of aeroelastic bodies, both in high-fidelity simulations and in experiments, shall be in the focus of our near future research. Our first results related to mechanical design and manufacturing of suitable experimental platforms are given in the section follow.

#### 4. Morphing wing segments

The main technical results are presented in this section. To validate experimentally the distributed modelling and control concepts, we develop related subscale experimental platforms suitable for wind tunnel testing. 3D printing is the technology used for mechanical design and rapid prototyping. Experimental morphing wing model is composed of discrete segments with the following construction requirements:

- Lightweight
- Flexible in axis perpendicular to the wing
- Stiff for compression
- Stretching resistance
- Simple for manufacturing
- Modularity

The first experiments have been done with 3D printed wing segments equipped with MFC. Two different designs (type A, type B) are shown in Figure 2 and Figure 3. Design of type A is more flexible than the type B in an axis perpendicular to the wing. However, type B in contrast with type A enable shaping in the wing axis. Two MFC strips were glued together and used for airfoil banding. This pair of actuators were tested in two configurations. In the first configuration, MFC formed the skin of the one side of the segment and caused only small and asymmetric airfoil deformation. In the second configuration with MFC placed in the plane of the chord line, the deformation was symmetric and more significant than in the previous case.

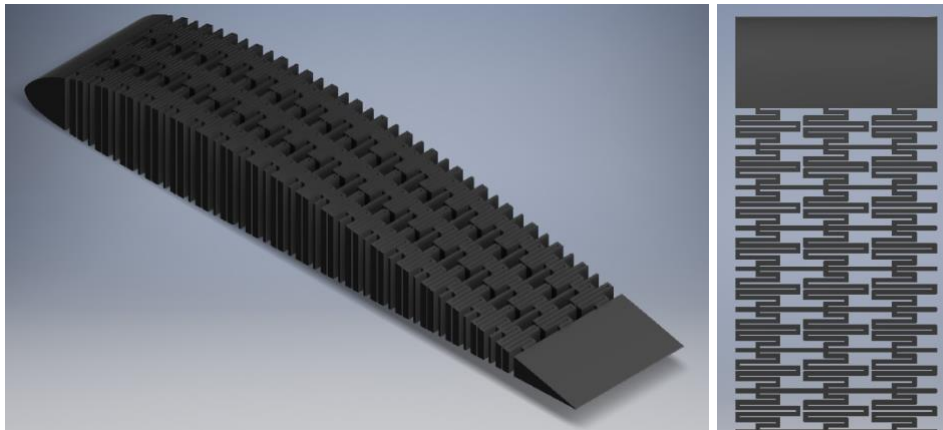


Fig. 4: Mechanical structure of the morphing wing segment - type A.

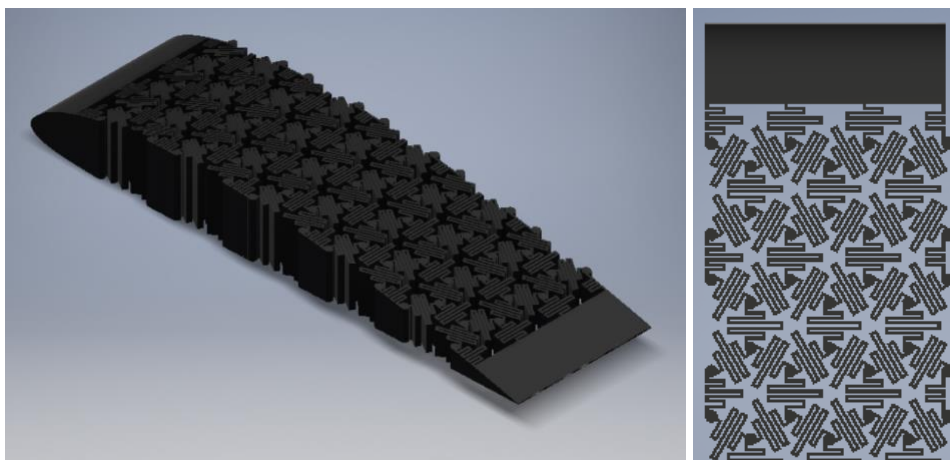


Fig. 5: Mechanical structure of the morphing wing segment – type B.

## 5. Conclusion

We present two wing segments designs, actuated by MFC in two different configurations. Similar architecture as we show in the structure A and the structure B will be used in future wing constructions, where the segments will be joined together and actuated independently. The possibility of airfoil morphing of individual wing segments offers new control approaches such as distributed control described in this paper.

## Acknowledgements

This work was supported by the Czech Republic Grant Agency grant No. 16-21961S.

## References

1. T. A. Weisshaar, Morphing aircraft systems: Historical perspectives and future challenges. *Journal of Aircraft*, vol. 50, pp. 337-353, 2013.
2. J. Hetrick, R. Osborn, S. Kota, P. Flick, and D. Paul, Flight testing of mission adaptive compliant wing, 48<sup>th</sup> AIAA/ASME/ASCE/AHS/ASC Structures, Structural Dynamics, and Materials Conference, 2007.
3. F. Svoboda, M. Hromcik, and K. Hengster-Movric, Distributed State Feedback Control for Aeroelastic Morphing Wing Flutter Suppression, 26<sup>th</sup> Mediterranean Conference on Control and Automation (MED), pp. 575-580, June 2018.
4. P. Husek, F. Svoboda, M. Hromcik, and Z. Sika, Low-complexity decentralized active damping of one-dimensional structures, accepted to *Shock and Vibration*, November 2018.

# AlGaIn/GaN HEMT heterostructures for gas- and bio-chemical transducers

B. Paszkiewicz, B.K.Paszkiewicz, M. Wosko, K. Indykiewicz, R. Paszkiewicz\*

Faculty of Microsystem Electronics and Photonics, Wrocław University of Science and Technology,  
Z. Janiszewskiego 11/17, 50-372 Wrocław, Poland  
\*Regina.Paszkiewicz@pwr.edu.pl

## **Abstract:**

The structure of the bio- chemical transducer was developed. It consists of a measuring element (sensor) combined with a reference element and is in a form of two transistors utilizing different control mechanisms: one with an electrolyte gate and the other one with a metal gate. This design allows for differential signal measurements, resulting in improving the sensitivity, as well as, thermal and long-term stability of the element. The transducer was fabricated in AlGaIn/GaN HEMT type heterostructure. The behaviour of the transducer in solutions with different pH was examined applying the custom developed methodology. Comparative investigations on the transistors with a metallic and electrolyte gate were carried out. For both of the measured transistors, the correct output and transient electrical characteristics were obtained. Furthermore, performed experiments showed that the transistor with electrolyte gate fabricated in AlGaIn/GaN HEMT heterostructure has good stability of pH sensing as well as good chemical resistance and suggest that the designed and fabricated device, is applicable as a bio- and chemical transducer.

## **Introduction:**

In recent years an increased interest in the application of nitrides materials for gas- and bio-chemical sensors is observed. In developed sensor two essential elements can be distinguished: transducer part and receptor part. As a result of analyte interaction with the receptor part, specific physico-chemical reactions occur causing changes in the properties of the transducer part. Depending on the type of applied transducer the chemical information is transformed into another type of energy in various forms of electrical, optical or acoustic signals. Typically, the semiconductor transducers utilize the field effect. It is the operation basic of MISFET (MOSFET), MESFET and HEMT transistors. Furthermore, these types of transistors could be used as transducers by replacing the metallic gate with receptor part. At the beginnings of transducer development, the silicon ISFET's transistors were used. In recent years, because of higher electrons mobility, the ISFET transistors were replaced by HEMT

transistors. Two-dimensional electron gas in the channel of HEMT's results in very high mobility, however classical AIII BV heterostructures, in which HEMTs are formed, are chemically and electrically unstable and could be biologically incompatible (or even toxic for cells cultures). Because of that issue, the AlGaN/GaN heterostructures that can be applied for this application, with different cap layers (AlGaN, AlN, GaN, SiN) were proposed for the HEMT fabrication process. Structure design is presented in Figure 1:

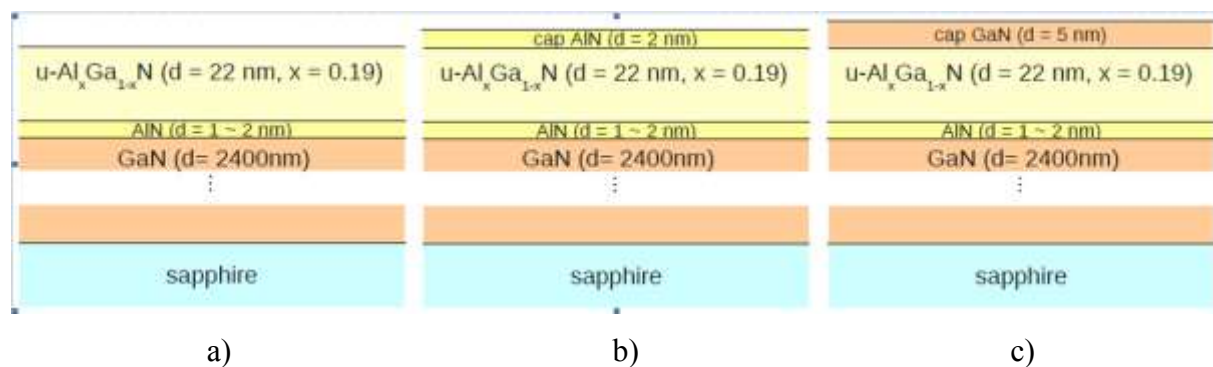


Fig. 1: The schematic layer structure of AlGaN/GaN HEMT-type heterostructures with different surfaces: AlGaN a), AlN b), GaN c)

The operation of AlGaN/GaN HEMT transistors is based on the modulation of the sheet carrier concentration of 2DEG (two-dimensional electron gas), in a triangular potential well, that is formed in the GaN layer on the AlGaN/GaN interface. The electrical response of AlGaN/GaN HEMT-type transducer that is observed could be: the change of the channel resistance, alteration of the drain saturation current or the change of the pinch-off voltage of the channel. Depending on the type of applied receptor layer the open-gated HEMT type AlGaN/GaN transducers could be used for sensing of various types of biological and chemical substances [1]. There was also found that the exposed surface of this type transducers is sensitive to pH changes of the electrolyte. It should enable elaboration of semiconductor pH sensor [2÷4]. The structure of the bio- chemical transducer was developed that consists of a measuring element (sensor) combined with a reference element in the form of two transistors utilizing different control mechanism: one with electrolyte gate and the other one with the metal gate. This design was selected because it allows differential signal measurements, that results in improving the sensitivity as well as the thermal and long-term stability of the element. The transducers were fabricated in AlGaN/GaN HEMT type heterostructure. The behaviour of the transducer in solutions with different pH was examined applying the custom developed methodology [5].

### **Transducers fabrication:**

HEMT's were fabricated in AlGaN/AlN/GaN heterostructures grown by MOVPE (Metalorganic Vapor Phase Epitaxy) technique on sapphire substrates in a low-pressure CCS 3x2" Aixtron system and were characterized using impedance spectroscopy method and Hall measurements. Mesa isolation of electrically active structures was achieved by RIE using Cl<sub>2</sub>/BCl<sub>3</sub>-based discharges. The ohmic contacts were made by lift-off of Ti/Al/Mo/Au metallization deposited in a single UHV process followed by optimized rapid thermal annealing (RTA). The Ru/Au Schottky contacts were evaporated by e-beam technique and formed in the lift-off process. Finally, the Ti/Au multilayer was deposited on the bonding pads of the ohmic and Schottky contacts. Thick polyimide layer was used for passivation of electrical structures and defining the electrolyte gate area. The counter electrode was fabricated by lift-off of Pt metallization. The wafers were encapsulated using SU8 except for the sensing region and electric pads. After dicing, the separate transducers chips were mounted and electrically connected to the specialized package.

### **Results and discussions**

A critical issue in the correct operation of the HEMT with a chemical gate is limited sensitivity and stability. In order to maximize its performance, test structures should include a measuring element (sensor) and a reference element. That can be realized by the pair of transistors that differ in their construction: a transistor with the electrolyte gate is used as an element that is sensitive to the presence of the detected substance and classical transistor with a metal gate that provide a reference signal. To obtain a stable reference signal, the development of a passivation technology for the biologically /chemically inactive part of the element is crucial. Requirements for the construction of the channel of the HEMT with a chemical gate are different from the structure of the transistor intended for use in the field of RF or gas sensing. The critical parameter of such a transistor is its transconductance, that is mainly influenced by the mobility of carriers and the choice of the point of its operation (operation in a linear or saturation regime).

The size of the active area also requires optimization. In developed transducer, special attention was paid to the problem of the layout of the source and the drain contacts. Due to the required long distance between the source and the drain, as well as the special design of the transistor in which contacts are spatially distributed, multilayer metallization connections were applied using polymer layers with a small dielectric constant. The contact pads were thickened electrolytically to withstand the high currents and mechanical loads expected. Two

sets of photolithographic masks were designed to fabricate devices test structures with various electrode configurations (HEMT type devices with different source-drain distance, presence/absence of a metallic gate). The measuring methodology of electrical parameters of the bio-chemical sensor transducers was developed [5] and measurements were carried out on the structures mounted in a specialized package. Figure 2 presents the optical microscope images of two types of bio- chemical sensing transducers fabricated in the AlGaIn/GaN heterostructures.

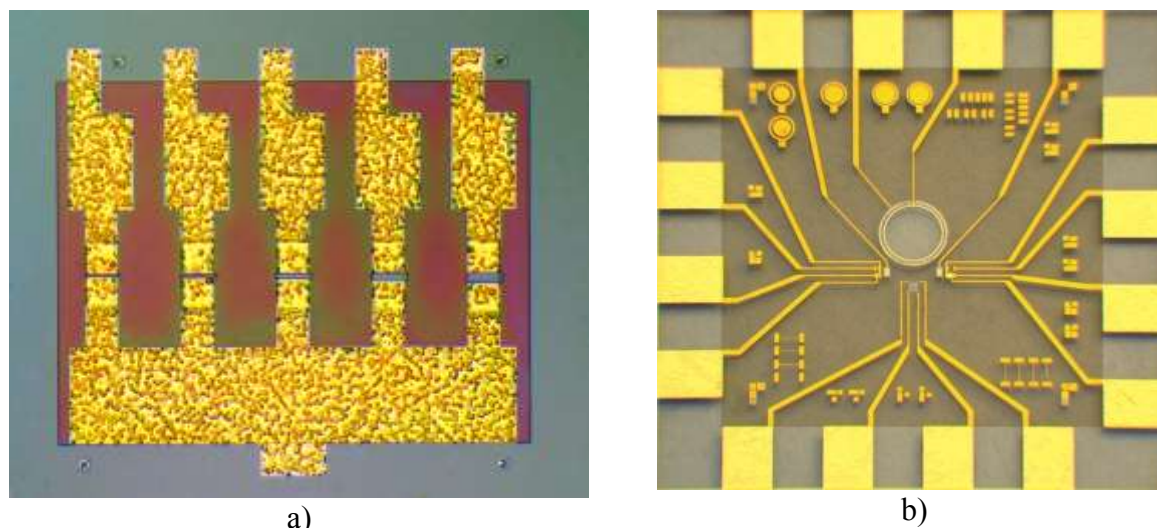


Fig. 2. Optical image of bio- chemical transducers developed in FMEP WUST: a matrix of 5 transistors with open gates of various lengths a), a structure containing 4 different types of transducers along with structures for devices technology testing b)

Figure 3 shows the SEM image of the part of the designed transducer chip: A-transistor with a metallic gate, B-transistor with an electrolyte gate, C-counter electrode. The whole structure, excluding the counter electrode and the area of the electrolyte gate, was covered with a polymer protective layer.

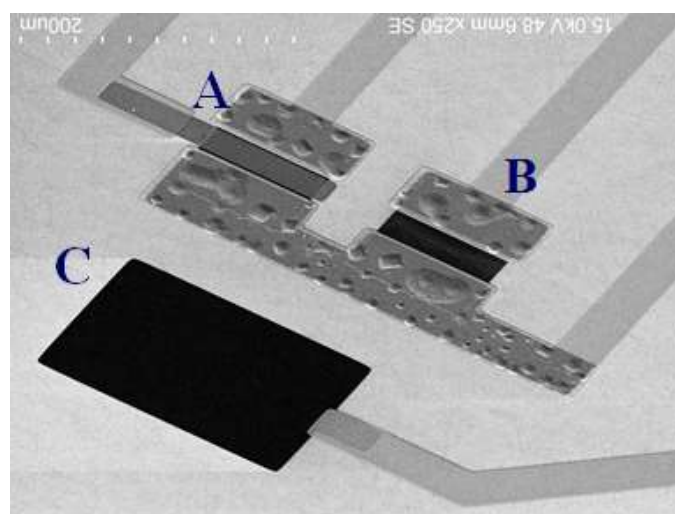


Fig. 3. SEM image of the designed transducer chip: A-transistor with metallic gate, B-transistor with electrolyte gate, C-counter electrode

The measurements of DC transistor characteristics with a metal gate and transistor characteristics with an electrolyte gate were performed in 1 molar aqueous KCl solution with different pHs, controlled by the addition of KOH or HCl. An external calomel electrode was used as the reference electrode. Figure 4 presents output characteristics of a transistor with a metallic gate (Fig. 4 a) and output characteristics of the transistor with an electrolyte gate in solutions of different pH (Fig. 4 b, c, d).

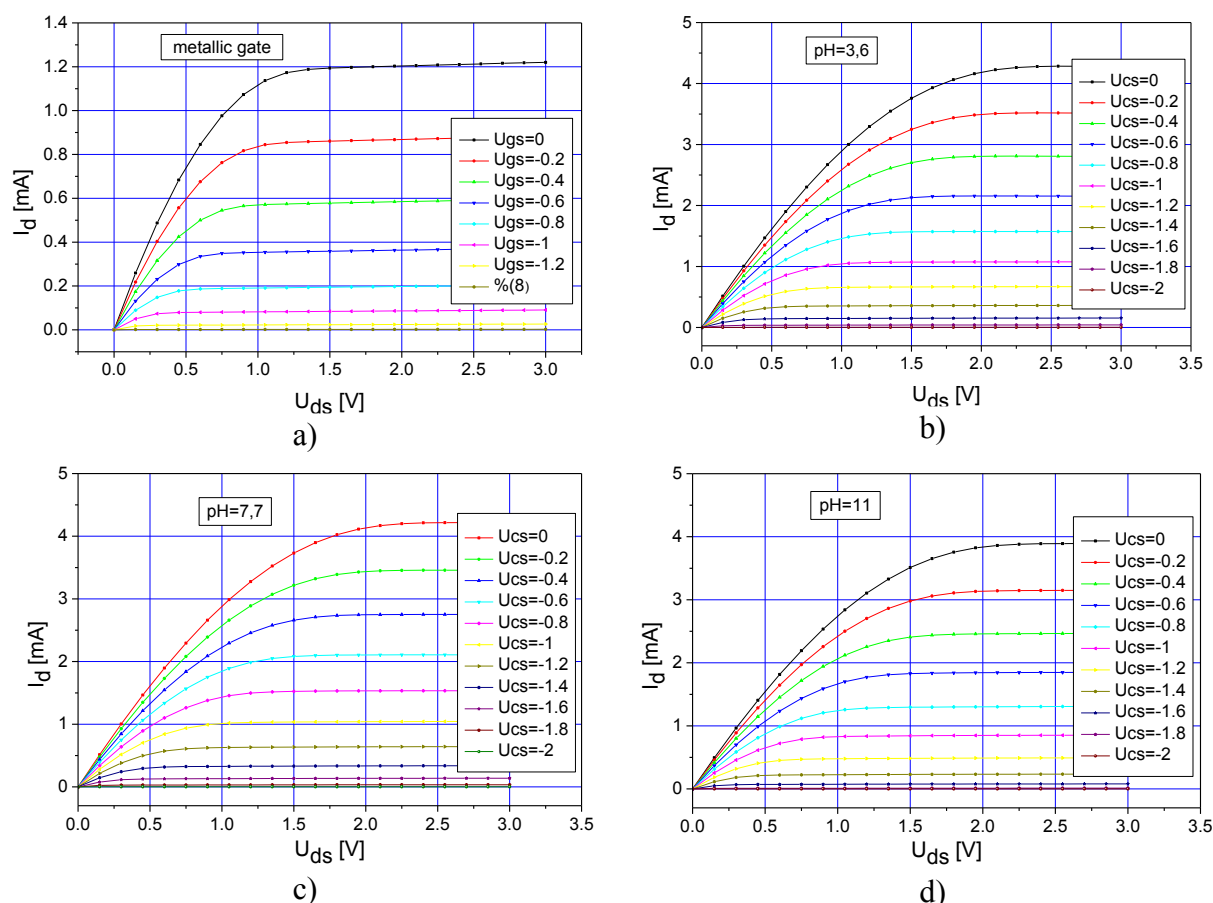


Fig. 4. The output characteristics of the transistor with a metallic gate a) and with an electrolyte gate (b ÷ d).  $I_d$ - drain current,  $U_{gs}$ - metallic gate-source voltage,  $U_{cs}$ -voltage between the counter electrode and source (for transistors with an electrolyte gate)

For each of the measured transistors, the correct characteristics were obtained. The observed difference in the value of the drain current occurring between the transistor with a metallic gate ( $I_d = 1.2$  mA) and the transistor with an electrolyte gate ( $I_d = 3.8 \div 4.3$  mA) results from different potential distribution in the examined structures. In the field effect transistor, the value of maximum saturated drain current is determined by the construction of the heterostructure, the length of the gate and the height of the potential barrier between the semiconductor and gate. In the case of the electrolyte gate the height of the potential barrier, between semiconductor and counter electrode, is influenced by the interactions between counter electrode-electrolyte and electrolyte-semiconductor. In the tested transducers, in the

case of electrolyte gates, the leakage current of the gate did not exceed 50 pA, while for transistors with a metallic gate was below 10 nA. The drain leakage current was comparable for both transistors and did not exceed 10 nA.

Figure 5 shows the transient characteristics of transistors with an electrolyte gate as a function of the potential difference between the reference electrode and the, source,  $U_{rs}$ , for three different pH values. In the same figure, the transient characteristic of the transistor with a metallic gate is also shown. For a transistor with a metallic gate  $U_{rs} = U_{gs}$ .

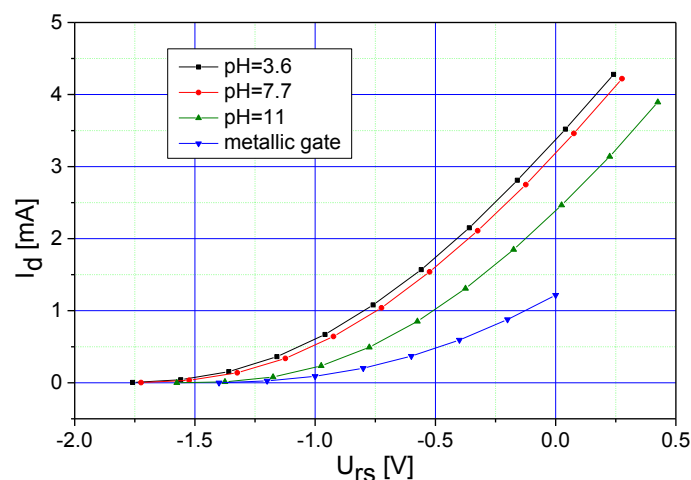


Fig. 5. Transient characteristics of transistors with electrolyte gates and a metal gate transistor ( $U_{rs} = U_{gs}$ )

The smaller values of the drain currents with a metallic gate could not be explained only by changing the contact potential difference between the gate and the semiconductor. Most likely, in the case of transistors with electrolyte gate, the length of the gate (open window in the thick polymer layer) is smaller than the length of the metallic gate. The change of dimension, in relation to the nominal dimension on the photolithographic mask, in the case of metallic layers fabricated using the standard lift-off metallization procedure, can be up to  $\pm 0.3 \mu\text{m}$ , while in the case of an electrolyte gate the size of windows open in thick photosensitive layers polymers, can be significantly different. In addition, in the case of an electrolyte gate, the formation of a strong electric field domain at the drain edge of the gate may be accompanied by other phenomena. In contrast to the equipotential metal gate, with a stable barrier, in the case of electrolyte, the height of the barrier will be influenced by the resulting double layer and surface chemical reactions, which will be further influenced by the electric field directed along the channel. Also, the effects related to the so-called "virtual gate" can affect the value of the drain current [6]. In the case of a metallic gate, gate loses, including

surface leakage, in the studied structures was more than two orders of magnitude larger and amounted to 10 nA. For the electrolyte gate, this value was 50 pA

Figure 6 shows the dependence of the drain current as a function of the pH of the solution ( $U_{rs} = 0$  V,  $U_{ds} = 2.7$  V, whereas Figure 7 shows the relationship of  $U_{rs}$  voltage as a function of solution pH for a constant value of drain current ( $I_d = 2$  mA) and drain-source voltage ( $U_{ds} = 2.7$  V).

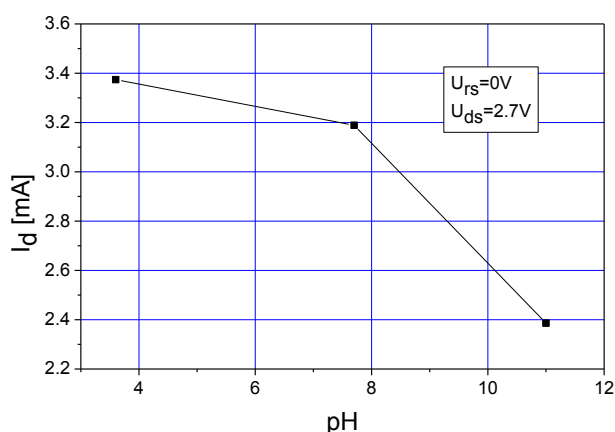


Fig. 6. Drain current dependence  $I_d$  as a function of the pH of the solution

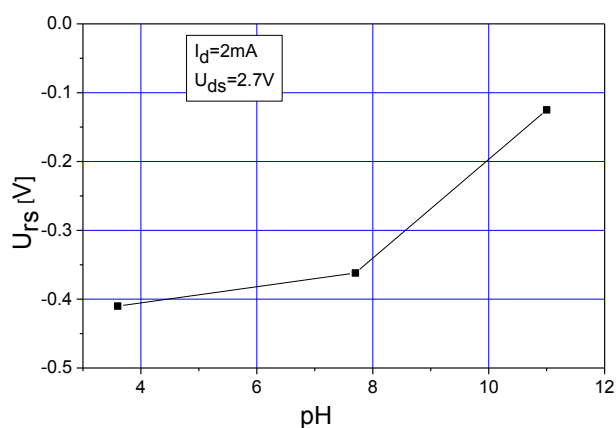


Fig. 7. Dependence of  $U_{rs}$  drain voltage on the pH of the solution

The shift of the transient characteristic (Fig. 5) was consistent with the measurement that shows the changes in the cut-off voltage of the transistor as a function of pH of the solution measured by non-destructive methods using impedance spectroscopy. The obtained consistency of results confirmed the correctness of the adopted methodology of metal-electrolyte contact research using non-destructive methods of impedance spectroscopy.

## Conclusions

The transducer was developed that consists of a measuring element (sensor) and a reference element. The design was proposed in a form of two transistors: one with electrolyte gate and the other with metallic gate. The transducer was fabricated in AlGaIn/GaN HEMT type heterostructure. The behaviour of the transducer in solutions with different pH was examined applying the custom methodology. Comparative investigations on the transistors with a metallic and electrolyte gate were carried out. For both of the measured transistors, the correct output and transient electrical characteristics were obtained. The difference in the drain current occurring between the transistor with a metallic gate and the transistor with an electrolyte gate ( $I_d = 1.2$  mA,  $I_d = 3.8 \div 4.3$  mA respectively) was observed and may stem from different potential distributions in the examined structures and/or the change of gates dimensions, in relation to the nominal dimensions on the photolithographic mask.

Furthermore, performed experiments showed that the transistor with electrolyte gate fabricated in AlGa<sub>N</sub>/Ga<sub>N</sub> HEMT heterostructure has good stability of pH sensing as well as good chemical resistance and suggest that the designed and fabricated devices are applicable for bio- and chemical sensing.

### **Acknowledgments**

This work was co-financed by the National Centre for Research and Development grants TECHMATSTRATEG No.1/346922/4/NCBR/2017, the National Science Centre grant No. DEC-2015/19/B/ST7/02494, Wroclaw University of Technology statutory grants and by the Slovak-Polish International Cooperation Program. This work was accomplished thanks to the product indicators and result indicators achieved within the projects co-financed by the European Union within the European Regional Development Fund, through a grant from the Innovative Economy (POIG.01.01.02-00-008/08-05) and by the National Centre for Research and Development through the Applied Research Program Grant No. 178782 and Grant LIDER No. 027/533/L-5/13/NCBR/2014.

### **Literature**

- [1] B. S. Kang, H. T. Wang, F. Ren, S. J. Pearton, Electrical detection of biomaterials using AlGa<sub>N</sub>/Ga<sub>N</sub> high electron mobility Transistors, *J. Appl. Phys.*, 104, 3, (2008), 031101.
- [2] M. S. Z. Abidin, A. M. Hashim, M. E. Sharifabad, S. F. A. Rahman, T. Sadoh, Open-Gated pH Sensor Fabricated on an Undoped-AlGa<sub>N</sub>/Ga<sub>N</sub> HEMT Structure, *Sensors*, 11, (2011), 3067-3077.
- [3] Liu, H.Y.; Hsu, W.C.; Chen, W.F.; Lin, C.W.; Li, Y.Y.; Lee, C.S.; Sun, W.C.; Wei, S.Y.; Yu, S.M., (2016), Investigation of AlGa<sub>N</sub>/Ga<sub>N</sub> ion-sensitive heterostructure field-effect transistors based pH sensors with Al<sub>2</sub>O<sub>3</sub> surface passivation and sensing membrane, *IEEE Sens. J.* 16, 3514–3522.
- [4] I. Sansalvador, C.D. Fay, J. Cleary, A.M. Nightingale, M.C. Mowlem, D. Diamond, D, Autonomous reagent-based microfluidic PH sensor platform. *Sens. Actuator B-Chem.*, 225, (2016), 369–376.
- [5] M. Hojko, D. Paszuk, B. Paszkiewicz, Measurement of AlGa<sub>N</sub>/Ga<sub>N</sub> heterostructure for sensor applications, *Optica Applicata*, 43, 1, (2013), 35-38.
- [6] S. Ghosh, S. Das, S. M. Dinara, A. Bag, A. Chakrabo, Off-State Leakage and Current Collapse in AlGa<sub>N</sub>/Ga<sub>N</sub> HEMTs: A Virtual Gate Induced by Dislocations, (2018), 1333-1339.

# Experimental investigation of the dynamic behaviour of Laminated Composite doped with graphene Nano additives using split Hopkinson pressure bars

M. Chihi<sup>1,2,\*</sup>, M. Tarfaoui<sup>1,3</sup>, A. El Moumen<sup>1</sup>, K. Lafdi<sup>3</sup>, C. Bouraoui<sup>2</sup>

<sup>1</sup> ENSTA Bretagne, IRDL - UMR CNRS 6027 Brest, France

<sup>2</sup> ENISO, Université de Sousse, BP 264, Cité Erriadh, 4023 Sousse, Tunisia

<sup>3</sup> University of Dayton, 300 College Park, Dayton, OH 45469-0256, USA

## **Abstract**

Since its advent in 2004, graphene has been one of the most promising materials in Nano-technology. This central role mainly stems from a combination of unique mechanical, electrical and thermal properties. Several research works have been carried out on the quasi-static behaviour of nanocomposites. However, high strain-rate loading experimental tests on such materials are essentially absent. This work examines and assesses the out-of-plane dynamic behaviour of polymer-laminated composites based on Epoxy resin, carbon fibres fabric and graphene nanoparticles. Specimens with two mass fractions, 0% as reference and 2% of graphene have been manufactured and tested. Dynamic compression tests were conducted using the Split Hopkinson Pressure Bars (SHPB) technique. Deformation histories and damage scenarios of specimens were recorded during dynamic compression by resorting to a high-speed camera. Experimental investigations have shown that the increase in the strain rate has a dramatic effect on the mechanical behaviour and the damage scenarios of the material. The effect of mass fraction of graphene on the dynamic properties and damage kinetics was discussed.

**Keywords:** Graphene, SHBP, Dynamic behaviour, Laminate Composites.

## **1. Introduction**

Since its advent in 2004 [1], graphene has opened new paths for developing a variety of novel functional materials [2]. It has been expected as the ideal reinforcement for polymer composites due to its unique graphitized plane structure, high aspect ratio, and low manufacturing cost. In order to achieve optimal improvement in the property of graphene/polymer composites, this strictly two-dimensional material has been incorporated into a wide range of the polymer matrix such as polystyrene [3], polyaniline [4], polypropylene [5], nylon [6] and epoxy [7] for various functional applications. Graphene-based polymer nanocomposites have shown higher thermal, electrical and mechanical properties compared to the neat polymer.

In a series of papers, El Moumen et al. [8-9] and Tarfaoui et al. [10-11] have investigated the effect of carbon nano-additive on the mechanical properties of polymers under static tests, In this study, the effect of the strain rate on the dynamic behaviour of laminated composite reinforced with graphene subjected to out-of-plane loading using SHPB is evaluated. Compression tests were conducted at two different strain rates; namely 765 s<sup>-1</sup> and 2358 s<sup>-1</sup>. The effect of the introduction of graphene on the dynamic properties of nanocomposites was discussed.

## **2. Experimental procedure**

### **2.1. Material**

The nanocomposite samples used in this study were made from 5 HS (satin) T300 6k carbon fibres fabric and graphene nanoparticles dispersed in Epon 862 Epoxy resin. Specimens with two mass fractions of graphene, 0% as reference and 2% of nanoparticles were manufactured and tested.

### **2.2. SHPB method**

The out-of-plane dynamic compressive tests were conducted using the Split Hopkinson Pressure Bar technique installed at the research centre of ENSTA Bretagne. This dynamic loading device is used to study the material behaviour under high strain rates. As shown by the schematic outlined in Fig. 1, the

SHPB apparatus is composed of a striker, an incident bar and a transmitted bar. Specimen was sandwiched between the incident/input and the transmitter/output bars without any attachment.

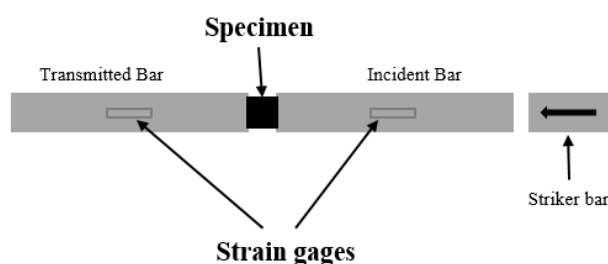


Fig. 1: Split Hopkinson Pressure bar apparatus

### 3. Experimental results

#### 3.1. Tests Repeatability

Dynamic compression tests in OP direction of graphene-based polymer nanocomposites were performed using the SHPB at strain rates ranging from  $765 \text{ s}^{-1}$  to  $2358 \text{ s}^{-1}$ . The evolution of the strain rate vs time of nanocomposite specimens with 2% mass fraction of graphene are shown in Figure 2. For each fraction of graphene, the test was repeated three times with the same impact pressure in order to ensure the reproducibility of the experimental data. It can be seen that all of the curves exhibit the same tendency.

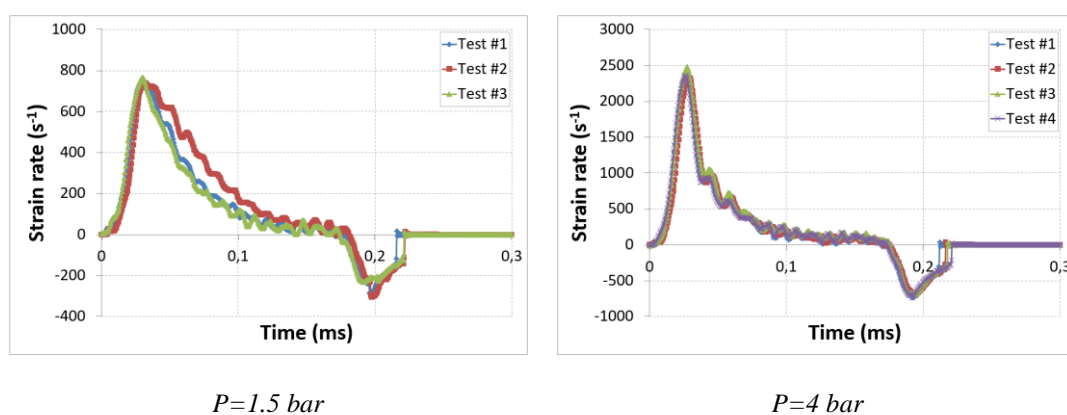


Fig. 2: Evolution of strain rate at different impact pressures, 2% of graphene

#### 3.2. Effect of Graphene incorporation

Nanocomposite specimens were subjected to out-of-plane loading with two different impact pressures 1.5 and 4 bars. Strain rate-time curves for samples with different amounts of graphene are shown in Figure 3. Clearly, the strain rate evolution is affected by the introduction of nanofillers. The addition of 2% of graphene provides a material, which exhibit more important, strain rate. The stress strain curve vs mass fraction of nanoparticles was presented in Figure 4 for the case of specimens subjected to 4bars. From this figure, it appears that the addition of 2% of graphene does not affect the dynamic behaviour of composites, especially the maximum stress.

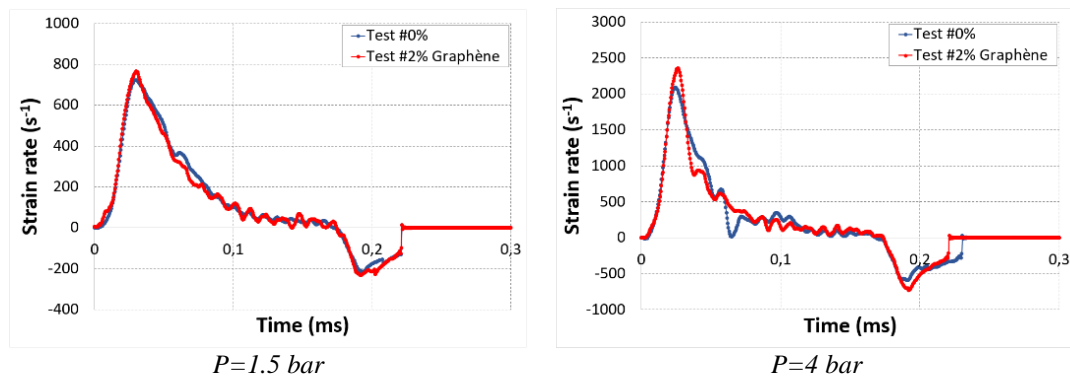


Fig. 3: Parameters under dynamic compression tests with various graphene mass fractions

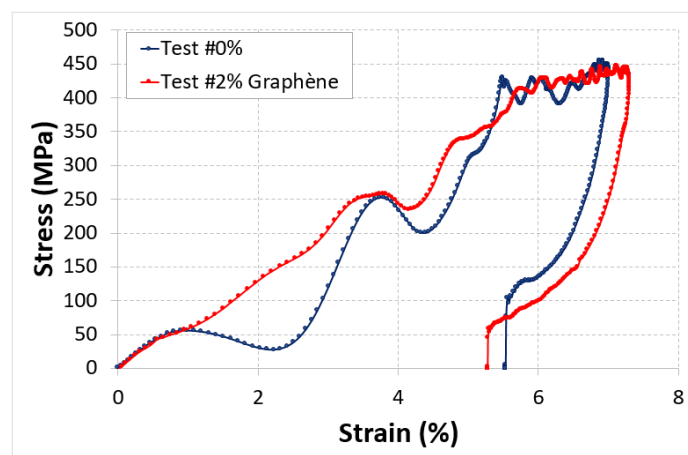


Fig. 4: stress-strain curves vs mass fraction of graphene, P=4bar

#### 4. Conclusion

This work was carried out in order to investigate the effect of graphene nanoparticles on the dynamic behavior of nanocomposites under dynamic compression at high strain rate. For that purpose, different specimens with two mass fractions were considered. The test was conducted with SPHB machine. It appears that the addition of 2% of nanoparticles does not affect the dynamic behavior of composites.

#### 5. References

- [1] K. S. Novoselov, “Electric Field Effect in Atomically Thin Carbon Films,”. *Science.*, vol.306, pp.666–669, 2004.
- [2] S. Park. “Chemical methods for the production of graphenes,” *Nat. Nanotechnol.*, vol.4, pp.217-224, 2009.
- [3] H. A. Pang. “The effect of electric field, annealing temperature and filler loading on the percolation threshold of polystyrene containing carbon nanotubes and graphene nanosheets,” *Carbon.*, vol.49, pp.1980–1988, 2011.
- [4] J. Yan. “Preparation of a graphene nanosheet/polyaniline composite with high specific capacitance,” *Carbon.*, vol.48, pp.487–493, 2004.
- [5] P. G. Song. “Fabrication of exfoliated graphene-based polypropylene nanocomposites with enhanced mechanical and thermal properties,” *Polymer.*, vol.52, pp.4001–4010, 2004.
- [6] R. Rafiq. “Increasing the toughness of nylon 12 by the incorporation of functionalized graphene,” *Carbon.*, vol.48, pp.4309–4314, 2010.
- [7] J. J. Liang. “ Electromagnetic interference shielding of graphene/epoxy composites,” *Carbon.*, vol.47, pp.922–925, 2009.
- [8] A. El Moumen. “Experimental Study and Numerical Modelling of Low Velocity Impact on Laminated Composite Reinforced with Thin Film Made of Carbon Nanotubes,” *Appl. Compos. Mater.*, vol.25, pp.309–320, 2018.

- [9] A. El Moumen. “Computational Homogenization of Mechanical Properties for Laminate Composites Reinforced with Thin Film Made of Carbon Nanotubes,” *APPL COMPOS MATER.*, vol.25, pp.569–588, 2018.
- [10] M. Tarfaoui. “Self-heating and deicing epoxy/glass fiber based carbon nanotubes buckypaper composite,” *J. Mate. Sci.*, vol. 54, pp.1351–1362, 2019.
- [11] M. Tarfaouia. “Progressive damage modeling in carbon fibers/carbon nanotubes reinforced polymer composites,” *COMPOS PART B-ENG.*, vol. 112, pp.185-195, 2017.

# Controlled pore tuning on freestanding graphene using focused ion beam and electron beam induced platinum deposition

Timur Ashirov<sup>1</sup>, Doolos Aibek uulu<sup>2</sup>, Kemal Celebi<sup>3</sup> and Ali Coskun<sup>1</sup>

<sup>1</sup>Department of Chemistry, University of Fribourg,  
Chemin du Musee 9, 1700 Fribourg, Switzerland, timur.ashirov@unifr.ch, [ali.coskun@unifr.ch](mailto:ali.coskun@unifr.ch)

<sup>2</sup>Computer and Electrical Mathematical Science and Engineering, KAUST,  
Thuwal, 23955, KSA [doolos.aibekuulu@kaust.edu.sa](mailto:doolos.aibekuulu@kaust.edu.sa)

<sup>3</sup>ETH Institute of Polymers, ETH Zurich,  
Zurich, 8093 Switzerland [kemal.celebi@mat.ethz.ch](mailto:kemal.celebi@mat.ethz.ch)

## Abstract

Since its discovery, graphene has been widely used in many potential applications. Being atomically thin, graphene has can be used for membranes with ballistic flow mechanics. FIB is a good tool for making uniform pores. However, for direct gas sieving or water desalination pores below 5 nm are required. Making such pores using FIB is challenging. For smaller pores fabrication TEM can be used, but it is limited to area and time consuming, which makes it not feasible for membrane applications. We have found an applicable way to tune pores below 5 nm using Pt electron beam induced deposition using FIB. Pt deposition reduces pore radius, controlling parameters will lead to pores below 5 nm.

**Keywords:** graphene membranes, nanopores, FIB, pore tuning, FIB Pt deposition, freestanding graphene

## 1. Introduction

Graphene being discovered in 2004 is utilized in many potential applications ranging from optoelectronics to membranes [1-3]. Interesting properties of graphene are mainly because of its atomic thickness. Also, due to this property has very high potential in conventional membrane applications. Firstly, in 2013 graphene has been utilized as a membrane and has shown extraordinary ballistic flow mechanics with very high permeance [2]. Since that usage of graphene as a membrane has become a viable topic of research [4-6]. Graphene is impermeable even to smallest molecules like He, that's why artificial pores need to be made. Different techniques and methods are applied for pore fabrication [7]. Among these techniques Focused ion beam (FIB) instrument allows controllable uniform and large area pore making. Based on source of ions used in FIB technique it is possible to make pores smaller close to 5 nm. Recently, it was reported that using high energetic Ga<sup>+</sup> ions uniform pores of 7-8 nm in diameter size and with He<sup>+</sup> ions 5 nm pores were opened [8]. For high selectivity applications like gas sieving and water desalination pores smaller than 5 nm sometimes, even below 2 nm pores are required. This is the challenging part as this is not achievable using FIB. Alternatively, Transmission electron microscope (TEM) can be for fabrication of pores smaller than 2 nm in diameter [9,10]. However, due its very small applicable scale, pore fabrication time it is not practical. Solution for making pores below 5 nm is controlled pore tuning. Graphene self-healing effect is known for more than five years [11]. Aspects of graphene self-healing effect has been studied both theoretically and shown practically [12,13]. However, self-healing process is itself deposition of amorphous junk carbon on surface of graphene [11]. Based on same phenomenon, previously we showed controlled narrowing of FIB fabricated pores via self-healing mechanism [14]. Using self-healing property of graphene, it was achieved pores smaller than 5 nm. Nevertheless, controlling pore radius is very challenging and deposited carbon is randomly oriented rather than two dimensional. Another method to narrow pore size using HfO<sub>2</sub> deposition in Atomic layer deposition tool was reported [15]. This technique was used to seal defects of graphene rather than pore tuning, as tuning is almost impossible to control in ALD due to reactions on specific sites.

Here we report a novel method for controlled graphene pores tuning using Electron beam induced platinum deposition (Pt EBID). Instead of depositing uncontrolled and amorphous junk we used Pt deposition using FIB instrument. Pt deposition in FIB is used mainly for fabrication purposes; due to this fact, controlling the deposition parameters is very easy and versatile. Using Pt deposition for graphene pores controlled tuning makes possible for making uniform pores smaller than 5 nm in diameter.

However, before membrane applications, graphene needs to be transferred clean and without tears. Most commonly used method is based on wet transfer using polymethylmethacrylate (PMMA). On the other hand, this method not practical due to hardness in fishing out, PMMA removal afterwards etc., thus does not give impressive results [16]. Instead of using conventional PMMA, we have used thick sacrificial layer of photoresist. By simple drop casting without spinning, the photoresist forms a thick layer above graphene, preventing fragility and enabling easy fish-out process from the metal-etch solvent. The resist layer can also be removed easily by acetone, not requiring extensive high temperature annealing under hydrogen [17].

## 2. Experimental

### 2.1 Materials and methods

Graphene was grown on low pressure chemical vapor deposition (LP-CVD) furnace on 25 μm thick copper substrate (Alfa Aesar). Temperature of growth was maintained as 1045 °C. 1000 sccm of H<sub>2</sub> gas was started to flow from the beginning of the procedure and it was stopped after furnace reached room temperature. Copper was annealed at 1045 °C for 50 minutes under hydrogen and 100 sccm of methane was flown for 5 seconds. Right after spotting methane supply furnace was started to cool down.

Graphene was transferred according to previously presented facile method [17]. First graphene on copper was coated with thick layer of Shipley S1200 photoresist (Dow Chemicals) and annealed at 70 °C in an oven for 12 hours. Copper was etched with ammonium persulfate solution (Merck). After few minutes of copper etching step, bottom layer of copper foil cleaned with dust free wipers and transferred to fresh persulfate solution. Continuing etching process, graphene samples were washed in deionized water (DI). Graphene was fished out to previously prepared silicon nitride frames [2]. Progressing the graphene to frame it was dried at room temperature for 30 minutes and photoresist layer was removed

with acetone. Prior to acetone removal step graphene on frame was baked on hot plate at 90 °C for better sticking. After complete removal of photoresist layer graphene sample was washed with isopropanol (IPA). Detailed schematics of facile graphene transfer method refer to SI.

SEM images were obtained with a field emission gun electron microscope at 5.0-15.0 kV and 0.40-0.58 nA current parameters (FEI Quanta FEG 200, FEI Czech Republic). High-resolution TEM images were obtained using FEI Technai Osiris instrument at 200 kV. AFM height measurements were done in Asylum Research MFP-3D model AFM instrument (Oxford Instruments). Height of Pt deposition was measured at tapping mode with a magnetic tip with nominal  $k=40$  N/m (Budget sensors,  $f=300$  kHz) at 0.50 Hz scan rate. All images and measurements were obtained at room temperature.

## 2.2 Pore fabrication and narrowing using Pt EBID

Uniform 10-30 nm sized graphene nanopores were fabricated using FEI FP 2067/30 Focused ion beam instrument by controlling dwell time, number of passes at 30.0 kV and 9.7 pA. Pores were narrowed using same instrument; electron beam induced Pt deposition was done at 5.0-15.0 kV and 0.40-0.58 nA current by controlling dwell time and number of passes.

## 3. Results and Discussion

### 3.1 Graphene transfer results

For many applications, especially for membrane production graphene needs to be transferred without tears, wrinkles and preferably clean [2,18]. Graphene samples transferred using new facile method were without tears, cracks, wrinkles and mostly clean (Figure 1A-C). Freestanding graphene samples were characterized with SEM. It is seen from the figure that graphene is perfectly standing without anything odd, except white dots, which are originated from CVD process [19]. Magnified and tilted images give better visual information about cleanliness morphology of freestanding graphene samples. Comparison between samples transferred with new facile method and PMMA is given in SI. It is obviously seen that new facile based method based on thick photoresist layer yields better results than conventionally used polymer method. Monolayer graphene was used further for fabrication purposes. Samples used for FIB pore making and further analysis.

### 3.2 Pore fabrication and tuning

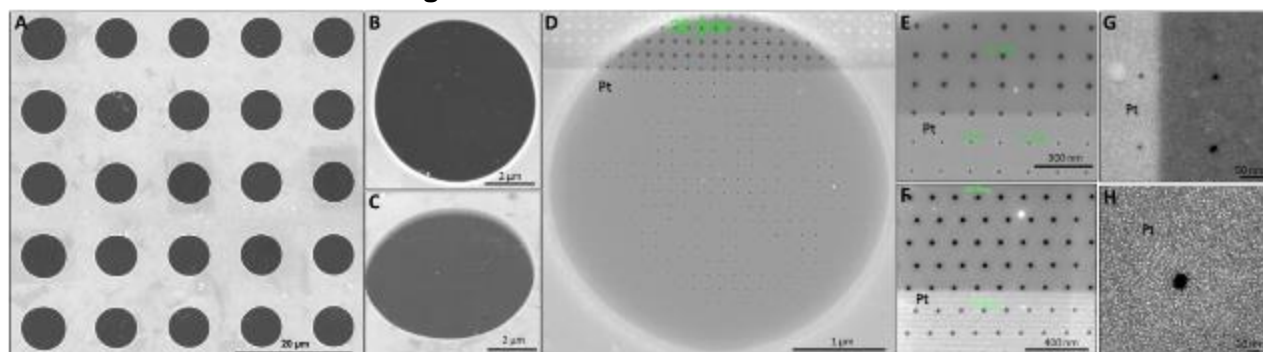


**Figure 1.** (A) SEM image of transferred graphene sample onto SiN<sub>x</sub> frame, here 5x5 6 μm pores are fully covered with graphene without any tears. (B) Close look SEM image of one of the pores. (C) 52° tilted SEM image of single SiN<sub>x</sub> pore covered with graphene, tilted images provide better information about morphology of graphene. (D) SEM image of pore perforated graphene with FIB and Pt deposited at 0.40 nA using 1 μs dwell time and 100 passes to narrow down pores (Pt deposited site is indicated with **Pt**). (E-F) Close look SEM image of graphene pores perforated with FIB and tuned with Pt EBID. (G) High-angle annular dark-field scanning transmission electron microscope image (HAADF-STEM) of graphene pores opened with FIB and narrowed using Pt EBID. (H) HAADF-STEM image of single perforated graphene pore tuned with Pt deposition.

Uniform different sized pores ranging from 10-30 nm were fabrication using different dwell time. Pores were characterized with SEM and after deposition they were recharacterized with HR TEM (Figure 1D-H). Smallest pores opened were 10-30 nm in diameter, which is limit for Ga<sup>+</sup> based FIB [8]. Deposited Pt layer covered the pores providing ability to controlled pore tuning. Initially, random parameters were chosen to test effect of pore tuning. On cleanly transferred freestanding graphene sample uniform 30 nm pores were opened, afterwards Pt was deposited. From the images, it is clearly seen that 30 nm pores almost halved. High-resolution TEM images confirmed pore size decrease.

### 3.3 Controlled pore tuning

After observation of pore tuning effect with Pt EBID, we decided to monitor its dependency with deposition parameters. Uniform 10-30 nm pores were fabricated in Ga<sup>+</sup> based FIB and Pt was deposited using 150, 250, 350, 450  $\mu$ s dwell time. Pore size reduction was calculated using ImageJ software. Accordingly, pore radius distribution before and after pore tuning was calculated and plotted in form of histograms (Figure 2), the number of passes kept constant.

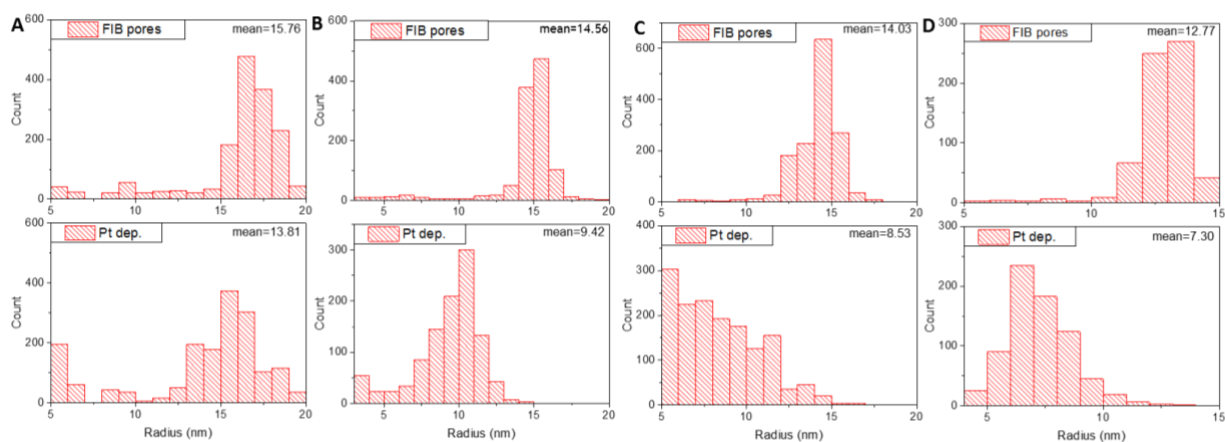


**Figure 2.** Histograms of pore size distribution before (top) and after Pt EBID tuning (bottom) at different deposition parameters; (A) Pores tuned using 150  $\mu$ s and 1 pass, (B) Pores tuned using 250  $\mu$ s and 1 pass, (C) Pores tuned using 350  $\mu$ s and 1 pass, (D) Pores tuned using 450  $\mu$ s and 1 pass.

Depending on Pt electron beam induced deposition parameters the pore size reduction also changed. Increasing dwell time leads to higher reduction in pore sizes, expectedly. Initially, pores fabricated with FIB were between 12-16 nm in radius, and after deposition of Pt they reduced to 7-14 nm. The highest pore size reduction was observed using 350 and 450  $\mu$ s dwell time during deposition. Pore size reduction can also be controlled by changing number of passes, however changing this will lead to higher thickness.

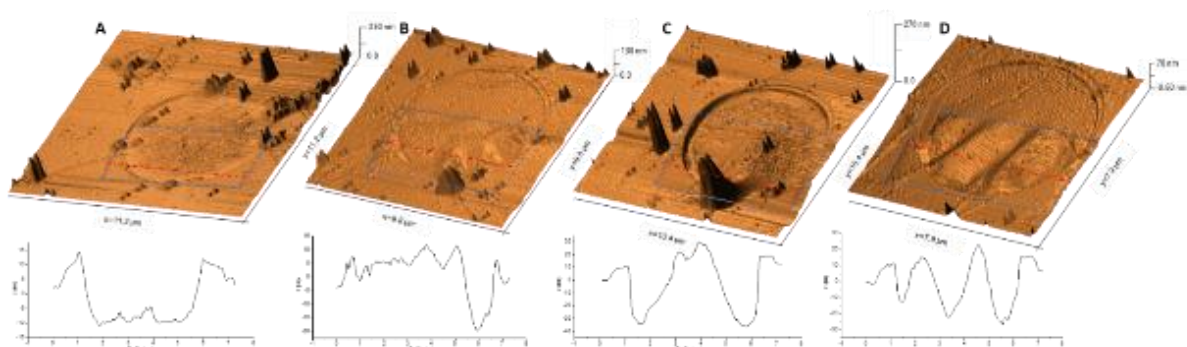


**Figure 3.** 3D AFM images (top) and height profile (bottom) of graphene pores fabrication with FIB and tuned using Pt EBID; (A) Pores tuned using 150  $\mu$ s and 1 pass, (B) Pores tuned using 250  $\mu$ s and 1 pass, (C) Pores tuned using 350  $\mu$ s and 1 pass, (D) Pores tuned using 450  $\mu$ s and 1 pass. Red line indicates where line profile was obtained and blue square shows Pt deposited area

### 3.4 Thickness of deposition

Thickness much depends on Pt EBID parameters. Deposited Pt layer thickness was measured using Atomic force microscope (Figure 3). According to results of AFM measurement, the thickness of Pt layer varied between 6-13 nm (Figure 4). It is so thin that, it is challenging to distinguish from AFM images the Pt deposited region. Increasing dwell time and number of passes theoretically leads to increase in thickness, expectedly. There is almost a linear relationship between height of Pt layer and

deposition parameters. Doubling dwell time almost doubles the thickness of deposited layer. The same relationship is observed while changing number of passes. As it is seen from the height profiles of AFM images, the thickness of Pt layer is not exceeding 15 nm (Figure 4).

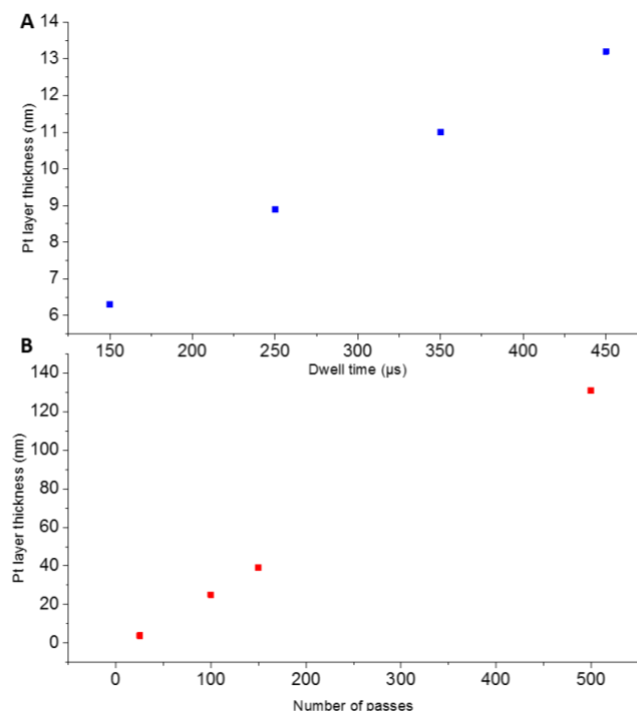


**Figure 4.** Pt layer thickness change with respect increasing dwell time (A) and number of passes (B). Increasing both parameters thickens the Pt layer expectedly.

Coming to uniformity of the Pt layer, it is mostly uniform but depends on freestanding graphene morphology. Pt deposition happens on top of graphene and takes graphene shapes. Freestanding graphene itself has a curvy structure leaning bottom from its center. Any junk or impurity beneath graphene forms bumps, as it covers the area as a carpet and takes shape of bump. Deposition can be controlled both using dwell time and number of passes. According to our observations, surface uniformity mainly depends on graphene morphology and slightly to deposition parameters. Keeping number of passes constant can form more uniform deposition rather than dwell time (refer to SI). Here also should be noted there is some minor parameters like pitch size, which has a noticeable effect on pore size reduction and thickness of deposited layer.

#### 4. Conclusion

These results show that Pt deposition can be used for controlled pore tuning to make pores smaller than 5 nm. Using proper conditions for Pt deposition and FIB pore fabrication, it is possible to make uniform pores beneath 5 nm. During graphene pore tuning the thickness of formed layer is not considered usually. However, this changes properties of graphene especially for membrane applications [2]. Here we have showed almost 100% pore size reduction using simple and on hand method using single instrument.

In addition, Pt deposition can be used to cover, close intrinsic tears, defects, holes or which formed during transfer process. Instead of depositing unknown amorphous carbon in an uncontrolled fashion, depositing Pt with full control and known negligible height provides more promising results. We hope this work will change the scope of CVD grown graphene and will open new areas of applications with extending existing ones.

#### Acknowledgments

We acknowledge prospective students Begimai Adilbekova and Khaydarali Sayfiddinov for their help during AFM measurements and production of SiNx membranes. We want to thank Prof. Coskun Kocabas from University of Manchester for his support during project progress.

## References

1. K. S. Novoselov, S. V. Morozov, D. Jiang, Y. Zhang, S. Dubonov, I. I. Grigorieva, and A. A. Fisov, “Electric Field Effect in Atomically Thin Carbon Films,” *Science*, vol. 306, no. 5696, pp. 666–669, 2004.
2. K. Celebi, J. Buchheim, R. M. Wyss, A. Droudian, P. Gasser, I. Shorubalko, J.-I. Kye, C. Lee, and H. G. Park, “Ultimate Permeation Across Atomically Thin Porous Graphene,” *Science*, vol. 344, no. 6181, pp. 289–292, 2014.
3. A. D. Ghuge, A. R. Shirode, and V. J. Kadam, “Graphene: A Comprehensive Review,” *Curr. Drug Targets*, vol. 18, no. 6, pp. 724–733, 2017.
4. A. Gugliuzza, L. Giorno, E. Drioli, *Graphene Membranes*. Encyclopedia of Membranes, 2015, pp. 1–6
5. H. W. Yoon, Y. H. Cho, and H. B. Park, “Graphene-based membranes: status and prospects,” *Philos Trans A Math Phys Eng Sci.*, vol. 374, no. 2060, p. 20150024, 2015.
6. X. Zhu, K. Yang, and B. Chen, “Membranes prepared from graphene-based nanomaterials for sustainable applications: a review,” *Environ. Science-Nano*, vol. 4, no. 12, pp. 2267–2285, 2017.
7. G. Liu, W. Jin, and N. Xu, “Graphene-based membranes,” *Chem. Soc. Rev.*, vol. 44, no. 15, pp. 5016–5030, 2015.
8. J. Buchheim, R. M. Wyss, I. Shorubalko, and H. G. Park, “Understanding the interaction between energetic ions and freestanding graphene towards practical 2D perforation,” *Nanoscale*, vol. 8, no. 15, pp. 8345–8354, 2016.
9. C. A. Merchant, K. Healy, M. Wanunu, V. Ray, N. Peterman, J. Bartel, M. D. Fischbein, K. Venta, Z. Luo, A. T. C. Johnson, and Drndić Marija, “DNA Translocation through Graphene Nanopores,” *Nano Lett.*, vol. 10, no. 8, pp. 2915–2921, Nov. 2010.
10. Schneider Grégory F., S. W. Kowalczyk, V. E. Calado, Pandraud Grégory, H. W. Zandbergen, L. M. K. Vandersypen, and C. Dekker, “DNA Translocation through Graphene Nanopores,” *Nano Lett.*, vol. 10, no. 8, pp. 3163–3167, Nov. 2010.
11. R. Zan, Q. M. Ramasse, U. Bangert, and K. S. Novoselov, “Graphene Reknits Its Holes,” *Nano Lett.*, vol. 12, no. 8, pp. 3936–3940, Oct. 2012.
12. T. Botari, R. Paupitz, P. A. D. S. Autreto, and D. S. Galvao, “Graphene healing mechanisms: A theoretical investigation,” *Carbon*, vol. 99, pp. 302–309, 2016.
13. H. Wang, K. Kurata, T. Fukunaga, H. Takamatsu, X. Zhang, T. Ikuta, K. Takahashi, T. Nishiyama, H. Ago, and Y. Takata, “A simple method for fabricating free-standing large area fluorinated single-layer graphene with size-tunable nanopores,” *Carbon*, vol. 99, pp. 564–570, 2016.
14. D. Aibek, T. Ashirov, K. Celebi, “Controlled Perforation of Freestanding Graphene by Focused Ion and Electron Beams” in *Graphene & Related Materials Conference (GRM-2016)*, Ankara, Turkey, 2016.
15. S. C. O’Hern, D. Jang, S. Bose, J.-C. Idrobo, Y. Song, T. Laoui, J. Kong, and R. Karnik, “Nanofiltration across Defect-Sealed Nanoporous Monolayer Graphene,” *Nano Lett.*, vol. 15, no. 5, pp. 3254–3260, 2015.

16. Y.-C. Lin, C.-C. Lu, C.-H. Yeh, C. Jin, K. Suenaga, and P.-W. Chiu, “Graphene Annealing: How Clean Can It Be?,” *Nano Lett.*, vol. 12, no. 1, pp. 414–419, 2011.
17. T. Ashirov, D. Aibek, O. Balci, N. Kakenov, C. Kocabas, K. Celebi. “A Facile Method for Clean Graphene Transfer Based on Sacrificial Photoresist Layers”, in *Graphene & Related Materials Conference (GRM-2016)*, Ankara, Turkey, 2016.
18. A. Banerjee and H. Grebel, “Freestanding Graphene and Its Applications,” *ECS Trans.*, vol. 19, no. 5, pp. 53–65, 2009.
19. X. Li, W. Cai, J. An, S. Kim, J. Nah, D. Yang, R. Piner, A. Velamakanni, I. Jung, E. Tutuc, S. K. Banerjee, L. Colombo, and R. S. Ruoff, “Large-Area Synthesis of High-Quality and Uniform Graphene Films on Copper Foils,” *Science*, vol. 324, no. 5932, pp. 1312–1314, Jul. 2009.